Distributed Extension across the Ethiopian Rift and Plateau Illuminated by Joint Inversion of Surface Waves and Scattered Body Waves

Jon Petruska[1] and Zachary C Eilon[2]

[1]University of California, Santa Barbara
[2]University of California Santa Barbara

November 22, 2022

Abstract

The East African Rift System provides a rare location in which to observe a wide scope of rifting states. Well-defined active narrow rifting in the Main Ethiopian Rift (MER) transitions to incipient extension and eventually pre-rifted lithosphere through the northwestern flank of the Ethiopian Plateau (EP). Although the MER is well studied, the off-axis region has received less attention. We develop Rayleigh wave phase velocity maps, Ps receiver functions, and H-$\varkappa$ stack surfaces, and jointly invert these data using a trans-dimensional, hierarchical Bayesian inversion algorithm to create shear velocity profiles across the MER and EP. All shear velocities observed are slower than the PREM global average, a reflection of the elevated temperatures that persist from plume impingement. In the EP, we find a shallow mantle slow shear velocity lineament parallel to the MER axis, amidst otherwise faster shear velocities. The crust is shallow in the MER, but also in the northwestern EP flank, with thicker crust found throughout the plateau caused by crustal underplating and flood basalt emplacement. Shear velocities more reduced than the already low regional average, in concert with surficial volcanic features, geodetic observations, and slow P- and S-wave anomalies, support off-axis extension in the Ethiopian plateau, requiring reevaluation of the localization of continental breakup in the narrow MER.

Distributed Extension across the Ethiopian Rift and Plateau Illuminated by Joint Inversion of Surface Waves and Scattered Body Waves

J. Petruska[1], **Z. Eilon** [1]

[1]Earth Science Department, University of California Santa Barbara, Santa Barbara, CA

Key Points:

- The Ethiopian Plateau's shear velocity structure is investigated by jointly inverting Rayleigh wave phase velocities and receiver functions.
- Slow off-rift shear velocities indicate elevated lithospheric temperatures in the Ethiopian Plateau that may require *in situ* melt.
- A slow axis-parallel lineament indicates off-rift extension in the Ethiopian Plateau, with increasing maturity towards its northern extent.

Corresponding author: Jon Petruska, `jonpetruska@ucsb.edu`

Abstract

The East African Rift System provides a rare location in which to observe a wide scope of rifting states. Well-defined active narrow rifting in the Main Ethiopian Rift (MER) transitions to incipient extension and eventually pre-rifted lithosphere through the northwestern flank of the Ethiopian Plateau (EP). Although the MER is well studied, the off-axis region has received less attention. We develop Rayleigh wave phase velocity maps, Ps receiver functions, and H-κ stack surfaces, and jointly invert these data using a trans-dimensional, hierarchical Bayesian inversion algorithm to create shear velocity profiles across the MER and EP. All shear velocities observed are slower than the PREM global average, a reflection of the elevated temperatures that persist from plume impingement. In the EP, we find a shallow mantle slow shear velocity lineament parallel to the MER axis, amidst otherwise faster shear velocities. The crust is shallow in the MER, but also in the northwestern EP flank, with thicker crust found throughout the plateau caused by crustal underplating and flood basalt emplacement. Shear velocities more reduced than the already low regional average, in concert with surficial volcanic features, geodetic observations, and slow P- and S-wave anomalies, support off-axis extension in the Ethiopian plateau, requiring reevaluation of the localization of continental breakup in the narrow MER.

Plain Language Summary

Ethiopia is a unique location where a continent is breaking apart, and will eventually evolve into a narrow ocean. Whether extension occurs only within narrow magmatic segments, or is broadly distributed elsewhere in Ethiopia has yet to be fully determined. To answer this question, we use information from earthquake-generated seismic waves to image the lower crust and mantle outside the expected bounds of continental breakup. We find evidence of extension well into the flanks of Ethiopia, in a rift-parallel linear band. This lineament shows more evidence of thermal affects associated with rifting in the north, suggesting it is more mature, or experiences a greater degree of rifting there. Elevated temperatures, volcanic features, small magnitude GPS measurements, and observations of slow material deep beneath the surface all indicate that extension is more complex, and more broadly distributed, than previously assumed, and that rifting processes are not localized to geographic areas where their surface effects are most visible.

Key Words Continental tectonics: Extensional, Africa, Surface waves and free oscillations, Tomography, Lithosphere

1 Introduction and Motivation

The Main Ethiopian Rift (MER), the northern segment of the East African Rift System (EARS), represents an intermediate state between unbroken continental crust and incipient seafloor spreading. Numerous studies have detailed the dynamics and evolution of this unique natural laboratory for extensional processes (Bastow et al., 2005; Julià et al., 2005; Dugda et al., 2007; Bastow et al., 2008; Keranen & Klemperer, 2008; Keranen et al., 2009; Rooney et al., 2012; Rychert et al., 2012; Ferguson et al., 2013; Armitage et al., 2015; Gallacher et al., 2016; Lavayssière et al., 2018; Chambers et al., 2019), and they agree on several key points. There exists widely distributed melt beneath the MER and nearby portions of the Ethiopian Plateau (EP). Fractional melt estimations vary from 0.5% to 10% (Guidarelli et al., 2011; Keranen et al., 2009; Gallacher et al., 2016; Chambers et al., 2019), but the presence of melt and elevated temperatures are required to achieve low observed velocities and anisotropy (J. O. Hammond, 2014) within the rift. Crust in the Northern and Southern MER is thinner than that of the Somalian Plateau or the EP (Mackenzie et al., 2005; Stuart et al., 2006; Maguire et al., 2006; Keranen et al., 2009; J. O. Hammond et al., 2011). Lastly, many agree that a mantle-sourced impetus in the form of a plume was necessary to initiate rifting the strong, thick Ethiopian lithosphere (Hayward & Ebinger, 1996; C. J. Ebinger & Sleep, 1998; Corti, 2009), which consequently caused widespread thermal perturbations, associated magmatism, crustal underplating, and uplift across Ethiopia. The scope of these previous geophysical studies have been primarily constrained to the MER axis, Afar, and the near-axis portions of the EP. However, geodetic data suggests that $\sim$20% - 30% of present-day extension may occur outside the magmatic segments of the MER (C. Ebinger & Casey, 2001; Birhanu et al., 2016), which begs the questions: where does this off-axis extension occur, and how is extension accommodated at depth?

In order to answer these questions, we interrogate the shear velocity structure of the lower crust and upper mantle in the EP and northwestern Ethiopian Plateau flank (NWEP) using a recently deployed broadband seismic array in conjunction with legacy data. We develop Rayleigh wave phase velocity maps, Ps receiver functions, and H-κ stack surfaces from teleseisms, and jointly invert these complementary data types using a trans-dimensional hierarchical Bayesian inversion algorithm (Eilon et al., 2018). We solve for shear velocity profiles beneath the EP, NWEP, and within the MER, and use these to support the existence of off-axis extension. We interpret shear velocity structure in the context of previous studies (*e.g.*, Dugda et al., 2007; Keranen et al., 2009; Chambers et al., 2019) and thermal structure associated with rifting.

2 Geological and Tectonic Background

Ethiopia has a complex tectonic and volcanic history that has shaped the evolution of the MER. Formed within the Mozambique Belt, Ethiopia preserves the Proterozoic-aged Himalayan style collision zone (Shackleton, 1986; Burke & Sengör, 1986) between East and West Gondwana, which scarred the basement with numerous sutures (Vail, 1985; Berhe, 1990; Stern et al., 1990), and Precambrian aged fractures (Korme et al., 2004). Some of these structures were reactivated in the Paleozoic-Mesozoic, creating ultimately aborted rifts (C. Ebinger et al., 2000; Mège & Korme, 2004; Corti, 2009), which left lithospheric weaknesses with the potential for exploitation by magmatic or extensional forces.

Within the MER, NW-SE trending strike-slip faults have reactivated to allow extension (Korme et al., 1997), demonstrating that existing fault structures control some degree of extension within the MER. NW-SE faults in the Ogaden basin and Blue Nile basin, which transect the EP and NWEP, reactivated from the early to late Jurassic and have interspersed lithospheric structures that may accommodate localized extension.

Thermal modification from impingement of the Afar plume and associated Tertiary volcanics have altered the lithospheric structure of the MER from that of the Mozambique Belt, which is believed to represent the pre-rift lithospheric structure of Ethiopia (Keranen et al., 2009). Plume related magmatism has exploited pre-existing weaknesses and fabrics in the lithosphere to produce a ∼1000 km diameter (Baker et al., 1996; Hofmann et al., 1997; Ukstins et al., 2002), 2 km thick region of flood basalts that cap much of the EP (fig. 1b).

Flood basalt emplacement began ∼45 Ma (Rooney et al., 2014), but was most prevalent between 31 - 29 Ma. Within the EP, shield volcanoes developed at 22 Ma and 10 - 7 Ma (Kieffer et al., 2004) (fig. 1b). Between 10 - 12 Ma, volcanoes appeared both within the MER and near Lake Tana (Abate et al., 1998; Conticelli et al., 1999; Kieffer et al., 2004). Present day fumaroles and thermal springs are active in both regions (fig. 1b). Quaternary volcanism is present in the form of Strombolian volcanoes and spatter cones South of Lake Tana (Kieffer et al., 2004), and along the Yerrer-Tullu Wellel Volcanotectonic lineament (YTVL), where clusters of volcanoes and fractures running E-W from the MER have erupted coevally with Northern MER volcanoes (Abebe et al., 1998; Chernet et al., 1998).

The MER is roughly outlined by Miocene aged border faults, and is trisected into Northern (NMER), Central (CMER), and Southern (SMER) sections. Rift initiation was asynchronous, with SMER volcanism beginning in 20 - 18 Ma (C. J. Ebinger et al., 1993; George & Rogers, 2002; Pik et al., 2008) and rifting following soon after at ∼18 Ma (C. J. Ebinger et al., 1993). The NMER then initiated ∼10 - 11 Ma (Chernet et al., 1998; Wolfenden et al., 2004), with accompanied volcanism. The CMER initiated last and exhibits a less evolved stage of rifting than the SMER and NMER, but its exact age is contested: between 5 and 9.8 Ma based on K/Ar dating (Woldegabriel et al., 1990; Bonini et al., 2005). Surface expressions of contemporary extension are largely localized to magmatic centers within the MER (C. Ebinger & Casey, 2001; Wolfenden et al., 2004), having shifted from strike-slip faults perpendicular to the rift axis that accommodated Quaternary extension (Korme et al., 1997). Composition of magmatic and basaltic samples indicate that the mantle beneath the MER and the nearby EP is hotter than the global average by 100° - 170° (Rooney et al., 2012; Armitage et al., 2015), and slow seismic velocities resolved here (Bastow et al., 2005; Benoit et al., 2006; Bastow et al., 2008; Keranen et al., 2009; Rooney et al., 2012; Rychert et al., 2012; Ferguson et al., 2013; Armitage et al., 2015; Gallacher et al., 2016; Lavayssière et al., 2018; Chambers et al., 2019) reflect this elevated temperature, and the consequent presence of melt.

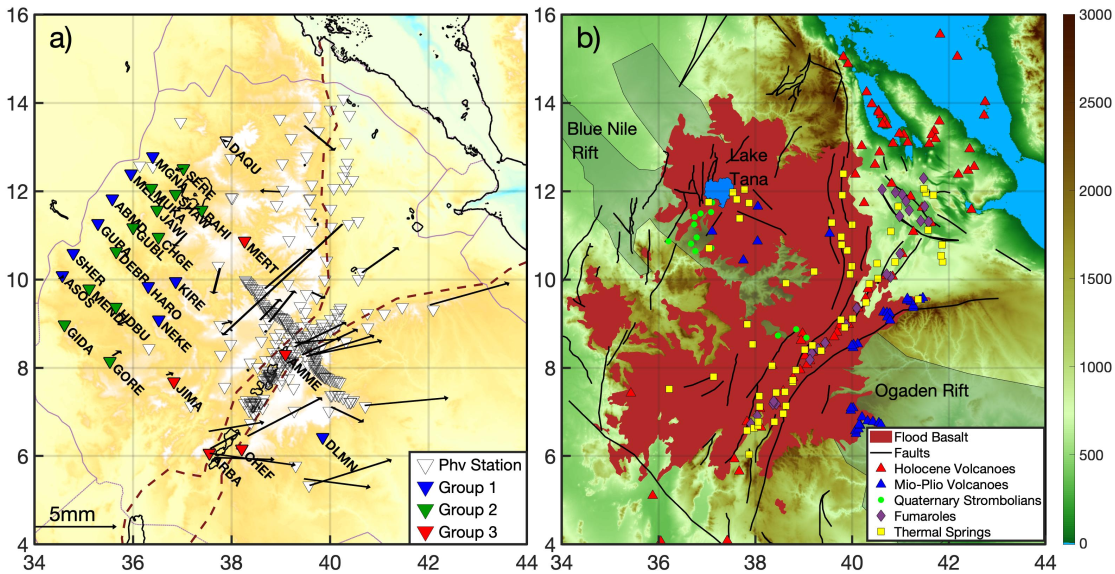

Figure 1: a) A map of all seismic stations used to develop phase velocity maps (triangles). Stations used to develop receiver functions, and that are inverted to develop shear velocity profiles are plotted in blue, green, and red, depending on their shear velocity group (see discussion). Stations plotted in white were used only for phase velocity measurements. Black arrows are GPS data from Birhanu et al. (2016). b) A map of relevant geology in the study area, colored by elevation (in m), showing flood basalt extent, geologically and currently active major faults, and a variety of volcanic and hydrothermal features.

3 Data and Methods

3.1 Phase Velocity Maps

Using the Automated Surface Wave phase velocity Measuring Systems (ASWMS) (Jin & Gaherty, 2015), we developed phase velocity maps from 25 s to 100 s using Rayleigh waves from teleseismic earthquakes. ASWMS autonomously estimates Rayleigh wave phase delays between nearby seismic stations using inter-station, frequency dependent cross-correlograms on a per-event basis. We used 5741 high quality earthquakes occurring between 2000-03-10 and 2017-10-03, of $Mw \geq$5.5, with a maximum depth of 250 km, at a distance of 30° - 160° from from the center of our study area (12°N 39.5°E). We processed vertical seismograms for all stations between 4°N and 20°N latitude, and 34°E to 45°E longitude (fig. 1a). Our data comprises 415 stations, and 17 public networks, a list of which and DOI's hosted by IRIS DMC are provided at the end of this manuscript.

We briefly explain the ASWMS methodology and quality controls used. For the full procedure, see Jin and Gaherty (2015). For each earthquake, vertical cross-correlograms, $C(t)$, were computed in the time domain for each possible station pair according to:

$$C(t) = S_1 \star W_S S_2 \tag{1}$$

where S_1 and S_2 are the de-trended, windowed, vertical seismograms of the two stations with instrument response removed, and $\star$ denotes cross-correlation. W_S is a 300 s windowing function, with a 75 s Hanning taper. $C(t)$ contains lag and coherency information about the Rayleigh wave energy travelling between the two stations. The dominant energy of the waveform was isolated using another windowing function, $W_c(t)$, and then filtered using a series of Gaussian narrow band filters. By fitting the filtered, windowed cross-correlogram function, $F_i{*}(W_c C(t))$ using a 5-parameter gaussian wavelet we extracted frequency-dependent phase delays, t_p, for this station pair (Jin & Gaherty, 2015).

Station pairs with inter-station distance (in km) less than 5, or greater than 3.55× the period (in seconds), were discarded to reduce the possibility of cycle skipping or spurious measurements. Station pairs with cross-coherency $\gamma^2 \leq 0.6$ were discarded to prevent measurement on poorly correlated cross-correlograms. t_p were then inverted using the Eikonal equation to develop inter-station phase travel time surfaces at each period (Lin et al., 2009).

ASWMS was initially designed for the large, evenly spaced US Transportable Array (Jin & Gaherty, 2015), use of this method for smaller arrays is feasible (Pratt et al., 2017; Jin et al., 2015; Orfanos et al., 2016) but requires careful quality control. As such, events for which more station pairs were discarded than not were also discarded from the stacks. We also culled regions within earthquake phase velocity maps that had apparent velocities below 3.25 km/s or above 4.6 km/s, as velocities outside these bounds are unrealistic for continental crust between 25 to 100 s (Oliver, 1962). We pieced together temporally and spatially isolated regions by stacking individual pixels from events. Pixels were included in the final stack if the number of rays crossing those pixels from all event maps exceeded 66 (providing on average one ray entering each pixel per km of circumference). Pixels in the same location between different events were assigned a weight, Wg, where $Wg = \frac{\text{\# of rays in event}}{\text{total rays}}$ such that events with a greater number of observations contributed more to the final stack phase velocity. Pixels with phase velocities more than two standard deviations from the stack mean were also excluded from the final stack. Maps were smoothed using a linear function with a lengthscale of 0.4 times the wavelength. The horizontal resolution of our phase velocity maps is approximately 2$\times$ the station spacing ($\sim$70 km) (Lin & Ritzwoller, 2011), in our case giving a maximum resolvable wavelength of 140 km.

3.2 *Ps* Receiver Functions

Receiver functions (RFs) were calculated from all Mw $\geq$5.5 earthquakes recorded on three-component broadband stations 30° to 90° from the approximate center of the study region (12°N, 39.5°E) between 2000-03-10 and 2017-10-03. 28 of these stations (fig. 1a) are used in further analysis, and can be found via station DOI's hosted by IRIS DMC at the end of this manuscript. Each 200 s seismogram trace spanned $\pm$100 s from the predicted P-wave arrival. Traces were de-meaned and bandpass filtered from 0.01 Hz - 0.25 Hz using a 2 pole Butterworth filter. We also culled events with a signal-to-noise (SNR) below 1.5, where signal and noise were computed as the maxima of envelope functions based on 8 s and 26 s smoothing of the whole trace, respectively. Waveforms were rotated into ZRT orientation and then migrated to the median ray parameter of the earthquake. We used the iterative time domain deconvolution technique (Ligorría & Ammon, 1999) to calculate receiver functions.

3.2.1 Receiver function quality control

On the basis of an *a priori* assumption that first-order crustal structure is one-dimensional, we assume that if a station has a family of highly similar RFs and another family of disparate RFs, the former is a faithful reflection of true crustal impedance structure, and the latter represent data anomalies that can be culled from the results. While strongly anisotropic crust or dipping layers may produce receiver functions with bimodal phase arrival times or strong back-azimuthal variations, we did not encounter this in our data.

We used a multi-stage process to select a family of receiver functions with similar waveforms, relying partly on the Density Based Spatial Clustering of Applications with Noise (DBSCAN) algorithm (Ester et al., 1996). DBSCAN is a path-specific hierarchical algorithm that uses two parameters to define clusters. The first is a distance metric, ϵ, which defines the maximum tolerable difference between two RF traces within the same cluster. The second is the minimum number of data to form a cluster, which we set as 30% of the number of RFs for a given earthquake.

Our quality control procedure comprised six steps: (i): We calculated the L_1 norm of the differences between all receiver functions for a given station (fig. 2a), and used those values as distances subject to ϵ. (ii) We used DBSCAN with a high ϵ (lenient) culling step on the RFs windowed narrowly around the expected P arrival, from T = 0 to T = 1.5s. This discriminated a cluster of RFs with "normal" P-wave arrivals from those with abnormal arrivals, which were discarded (fig. 2b). (iii) We culled receiver functions with amplitudes less than 0.5$\times$ the mean amplitude at T = 0. (iv) RFs that passed these culling steps were again processed using DBSCAN, this time with a time window from T = 2s to T = 15s, which included the Ps and $PpPs$ arrival phases for most receiver functions. We excluded the $PpSs + PsPs$ phases in this clustering step as they generally had lower amplitude arrivals. Within this step, we changed ϵ until a cluster of RFs were found that displayed the Ps arrival phase, and were stable when varying ϵ. (v) After a cluster of RFs were found, we culled traces with crustal multiple phase amplitudes greater than 30% of the trace's P arrival amplitude. (vi) Finally we visually assessed each station's RFs, and culled RFs that deviated substantially from the others (fig. 2c). The stacked receiver function (fig. 2d) used in the joint inversion algorithm was the linear mean of the 'cleaned' receiver functions that passed the above quality controls. 5 stations of original 33 within the study region were removed by visual flagging and not inverted in the joint inversion process.

3.3 H-κ Stacks

Receiver functions that passed the "cleaning" process were used in a standard H-κ stacking procedure (Zhu & Kanamori, 2000) to estimate crustal thickness and Vp/Vs ratio. We used a Vp of 6.3 km/s, and phase weights of 0.7, 0.2, and 0.1 for the Ps, $PpPs$, and $PpSs+PsPs$ phases, respectively. The resultant H-κ stack for each station was used to constrain crustal thickness during joint inversion (Section 3.4). H-κ stacks for each station are provided as a zipped supplementary file. Because κ values are consistently less well resolved than crustal thickness, we place little weight on them in our results discussion.

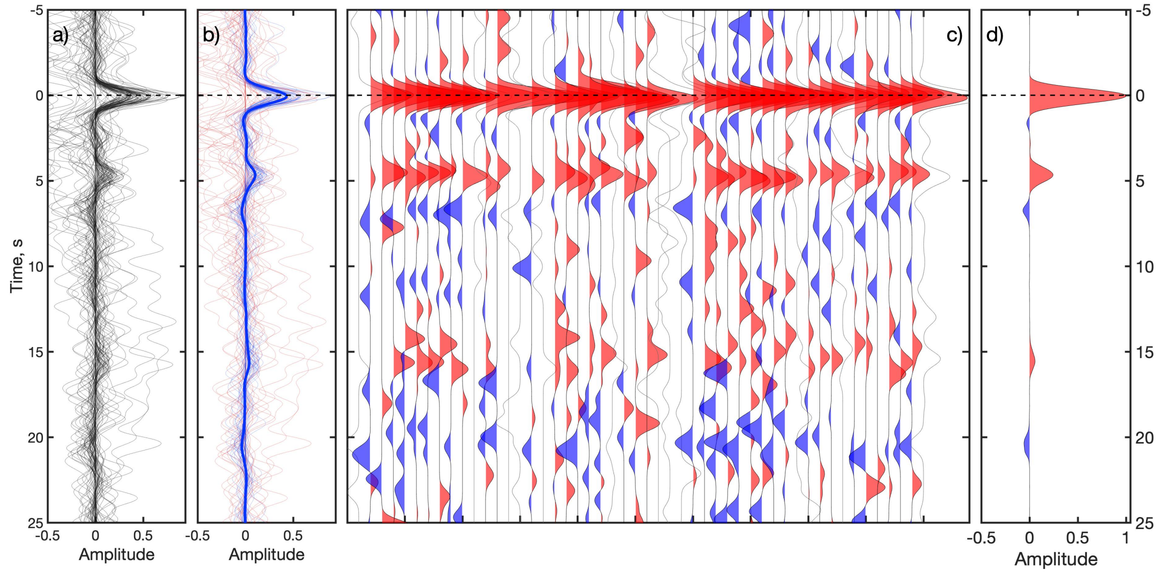

Figure 2: A graphical representation of the steps in our quality control process at station KIRE. a) The 104 raw receiver functions. b) The results of stages (i) and (ii) of the quality controls. Thin red lines are receiver functions culled by DBSCAN, thin blue lines are receiver functions passing quality controls, and the thick blue line is the mean of the clustered receiver functions. c) The manual visualization and cull step (vi) after clustering. Traces with colored red and blue fills, signifying positive and negative phases, were used for the final stack, others were manually removed. d) The final stacked receiver function from the 38 receiver functions that passed quality control, normalized to the parent phase amplitude.

Ogden et al. (2019) found that many H-κ derived crustal thickness and Vp/Vs ratio estimates were unreliable within the EP. Using an automatic method to perturb input parameters for H-κ stacking, they found that stations within flood basalts produced unreliable H-κ stacks with high standard deviation, low SNR, and broad, low amplitude arrival phases. Such H-κ stacks failed to resolve a high energy maximum for the Moho and κ due to a gradational Moho, complex crust, or sediments and basalts. We performed a modified version of Ogden et al. (2019)'s random input perturbation procedure on several stations in the region using receiver functions from before the quality control process and those that passed the quality control process. An example of this test may be found in fig. S11. From our results, we believe coherency between receiver functions is a good indicator of simple subsurface structure, and receiver functions that were culled exhibited receiver-side signal-generated noise. We found that a distinct high energy maximum was able to be well resolved after quality control for most stations (26 of 28), and be moderately resolved for the rest. We note that strong anisotropy may impact the H-κ process, or might cause the quality control algorithm to reject back-azimuthal swaths. However, while our earthquake arrivals are not uniformly distributed, we do not find evidence of systemic back azimuthal patterns or automatic rejections.

3.4 Joint Inversion Algorithm

In order to create shear velocity profiles that resolve lower crustal and mantle structure, we used a trans-dimensional, hierarchical, Bayesian inversion algorithm (Eilon et al., 2018). This algorithm uses Bayesian statistics and Monte Carlo Markov Chains to explore the model space, developing ensembles of shear velocity models that closely predict observed Rayleigh wave phase velocities and receiver functions. To ensure we adequately explored the parameter space, we ran 6 parallel Markov Chains for 21,000 iterations, approximately 16$\times$ the number of iterations required for a given chain to achieve stationarity (the "burn-in"). Proposed model updates were made by drawing from local Gaussian distributions for single parameters in each iteration. Model perturbations were accepted or rejected using a Metropolis-Hastings acceptance criterion (Metropolis et al., 1953; Hastings, 1970), and were confined by *a priori* distributions of seismological parameters. We adapted the method of Eilon et al. (2018) to incorporate H-κ surfaces as an additional data type. To some extent, this step simply increases the power of the RF data within the joint inversion. However by implicitly migrating crustal multiples in a more self-consistent manner than in a synthetic RF stack, it sharpens the inversion's constraints on crustal Vp/Vs ratio, for essentially zero increased computational expense.

We assumed that errors between different data types are uncorrelated (Khan et al., 2011; Drilleau et al., 2013; Shen et al., 2013; Bodin et al., 2016; Calò et al., 2016; Roy & Romanowicz, 2017), so the overall model likelihood function is computed as the product of likelihoods for each individual data type:

$$p\left(\mathbf{d} \mid \mathbf{m}\right) = \prod_i p\left(\mathbf{d}_i \mid \mathbf{m}\right) = \prod_i \frac{1}{\left(\sigma_i\sqrt{2\pi}\right)^{n_i}} \exp\left(-\frac{\Phi_i}{2\sigma_i^2}\right) \tag{2}$$

where σ_i is the data error for data type $\mathbf{d}_i$, n_i are the degrees of freedom, $\mathbf{m}$ is the proposed model, and Φ_i are misfit functions for body waves, surface waves, and H-κ surfaces, respectively, as follows:

$$\Phi_{\mathrm{BW}}(\mathbf{m}) = \left\|\mathbf{z}_p(t,\ \mathbf{m}) * \mathbf{R}(t) - \mathbf{r}_p(t,\ \mathbf{m}) * \mathbf{Z}(t)\right\|^2 \tag{3}$$

$$\Phi_{\mathrm{SW}}(\mathbf{m}) = \left\|\mathbf{C}(f) - \mathbf{c}_p(f, \mathbf{m})\right\|^2 \tag{4}$$

$$\Phi_{\mathrm{H}\kappa}(\mathbf{m}) = \frac{\eta_{max}}{\eta(H_p, \kappa_p)} \tag{5}$$

where $\mathbf{R(t)}$ and $\mathbf{Z(t)}$ are the radial and vertical observed time series of stacked receiver functions, $\mathbf{r}_p$ and $\mathbf{z}_p$ are corresponding predicted time series, and $*$ is the convolution operator. Note that this "cross-convolution" body wave misfit equation does not require synthetics to match the true source time function (Menke & Levin, 2003; Bodin et al., 2014). $\mathbf{C}$ and $\mathbf{c}_p$ are the phase velocity observations and predictions at frequency f. η is the amplitude of the H-κ surface, and H_p, κ_p, are the proposed model Moho thickness and Vp/Vs ratio.

Body wave data were forward modeled using a propagator matrix code (Keith & Crampin, 1977c, 1977a, 1977b) which creates synthetic Z,R,T waveforms from a 1-D layered input velocity model. We used a 1-s gaussian synthetic source time function and a ray parameter averaged from the RFs in the station stack. Only the first 10 seconds of RFs were used, which contain the P and Ps arrival phases. Surface wave phase velocities were forward modeled using MINEOS from CIG (Computational Infrastructure for Geodynamics) (Masters et al., 2007). MINEOS is computationally expensive, so data prediction relied on perturbation kernels calculated infrequently (and updated per Eilon et al. (2018) using MINEOS whenever the current accepted model departed substantially from the most recent kernel basis model). Because MINEOS requires a whole Earth model, our models linearly graded into the PREM global model (Dziewonski & Anderson, 1981) between 200 km and 300 km, and basal knots were prevented below 160 km to ensure no unrealistic sharp velocity gradients were involved in grading into the global velocity average.

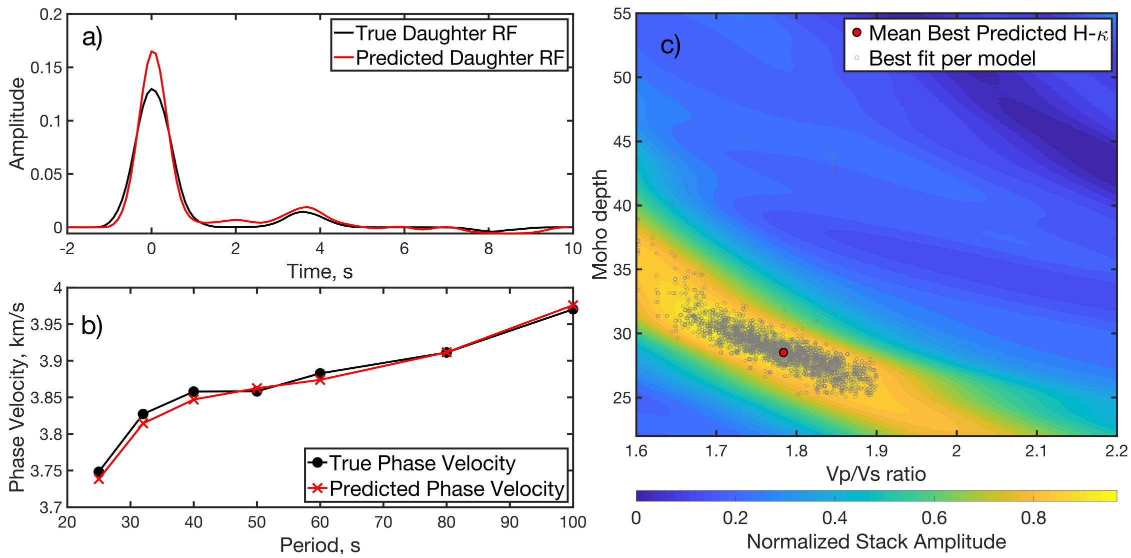

Figure 3: An example of the joint inversion data types at station GUBA, including final data fit. a) Stacked P-wave radial receiver function (black). The predicted receiver function computed from the mean posterior shear velocity profile following inversion is shown in red . b) Rayleigh wave dispersion curve at this station (black), together with MINEOS-predicted phase velocities from the mean posterior shear velocity profile (red). c) H-κ amplitude surface (η), with the corresponding values from the entire posterior model ensemble (light grey dots), and the mean of this posterior (red dot).

3.5 Shear Velocity Aggregate Groups

On the basis of the observed shear velocity profiles (Section 4.3), we determined that stations could be assimilated into three characteristic groups. We started off with three random groupings of stations. For 1000 iterations, we randomly moved a single station to a different random group. We then calculated the summed absolute misfit between individual profiles and their group mean $V_S(z)$, and added the total misfit across all the groups. If this misfit decreased from the previous iteration, indicating overall more similar intra-group velocities, we accepted the new group assignment. In this way we established three groups of stations. Station AMME (8.3031°N, 39.0934°E) was manually placed into group 3 because of its location in the MER instead of group 2, to which the shear velocity structure more closely matches. For this analysis, we ignored station DAQU (13.1448°N, 37.8976°E) which had a shear velocity structure that does not closely match any groups, despite the inversion yielding a good data fit. Finally, we calculated mean shear velocity profiles and 37%, 67% percentiles for all three groups.

4 Results

4.1 Phase Velocity Maps

Phase velocities in the NMER and SMER are slow from 25 - 80 s (fig. 4a), and follow the surficial border faults of the MER to 32 s. The CMER is up to 0.1 km/s faster than the SMER and NMER from 32 - 60 s, but remains slower than the EP and Somalian Plateaus. Slow velocities in the MER asymmetrically broaden into the EP with increasing period, extending less into the Somalian Plateau. By 80 s, the MER, the Somalian Plateau, and eastern EP homogenize to phase velocities of 3.75 - 3.8 km/s, which remain reduced compared to the western EP.

Slow phase velocities extend in a lineament east-southeast from Lake Tana at periods of 25 - 60 s (fig. 4a - e). This lineament roughly follows the trend of late Paleozoic-Mesozoic aged rifts (Mège & Korme, 2004), Quaternary volcanoes, and spatter cones (Kieffer et al., 2004). Phase velocities here are ∼0.1 km/s faster than the MER at 25 s (∼3.5 km/s, vs. 3.4 km/s). In the north, this structure links to slow phase velocities at the western boundary of Afar from 25 - 32 s. This structure grades into less reduced, but still slow, phase velocities to the southwest between Lake Tana between 25 - 50 s. This slow phase velocity lineament does not broaden with period, and homogenizes to the fast background NWEP phase velocity by 80 seconds.

A pronounced ∼200 km E-W, ∼160 km N-S, fast phase velocity region in the central EP at 32 s separates the slower phase velocities in the MER and EP lineament (fig. 4b). Velocities here are ∼4.0 km/s, ∼8% faster than the ∼3.7 km/s area average at 32 s. This appears to result from a shallow feature: the phase velocities in this location are not noticeably slower than the regional average beyond ∼50 s, although at longer periods most of the EP and flank are ∼0.1

km/s faster than the study region average. Fast phase velocities also exist in the Somalian Plateau from 25 - 50 s ($\sim$3.7 - 3.9 km/s). At periods >60s, the phase velocities on either side of the MER are roughly symmetrical and the rift-proximate part of the Somalian plateau that we image is clearly slower than the rift-distal NWEP.

4.2 Receiver Functions

The number of total receiver functions at each station varied between 9 - 165, and averaged 65. The fraction of receiver functions culled by our automatic quality controls averaged 51%, and ranged between 26 - 82% of recorded traces. On average, manual culling removed a further $\sim$16% of traces. The number of RFs that passed quality controls to develop the final stacked RF varied from 2 - 73, with a mean of 23. The quality control process summarized in fig. 2 may be found for each inverted station in a zipped supplementary file.

All receiver functions show a distinct Ps phase arrival $\sim$5 s after the parent phase (fig. 2d), and 25 show a clear $PpPs$ phase arrival (fig. 2d, $\sim$16 s). 21 stations displayed a $PpSs + PsPs$ arrival phase (fig. 2d, $\sim$21 s), which was often broader and lower amplitude than preceding phases, potentially caused by stacking across moveout, or more local issues outlined in Ogden et al. (2019), including non-simple crustal structure, gradational Mohos, or flood basalts overlaying sediments.

A negative phase following the Ps arrival is observed at 16 stations (*e.g.*, fig. 2d, $\sim$6 s). All group 1 station RFs record this phase, but it does not arrive at a consistent time. It is absent from all group 3 stations except AMME, where it immediately follows the Ps phase, and has a large negative amplitude. More rigorous investigation of these negative velocity gradients, which may link to intra-lithospheric layering (Abt et al., 2010), will be the subject of future work. Because of the time window used for RFs in joint inversion, these phases must also be accounted for in the body wave forward modelling.

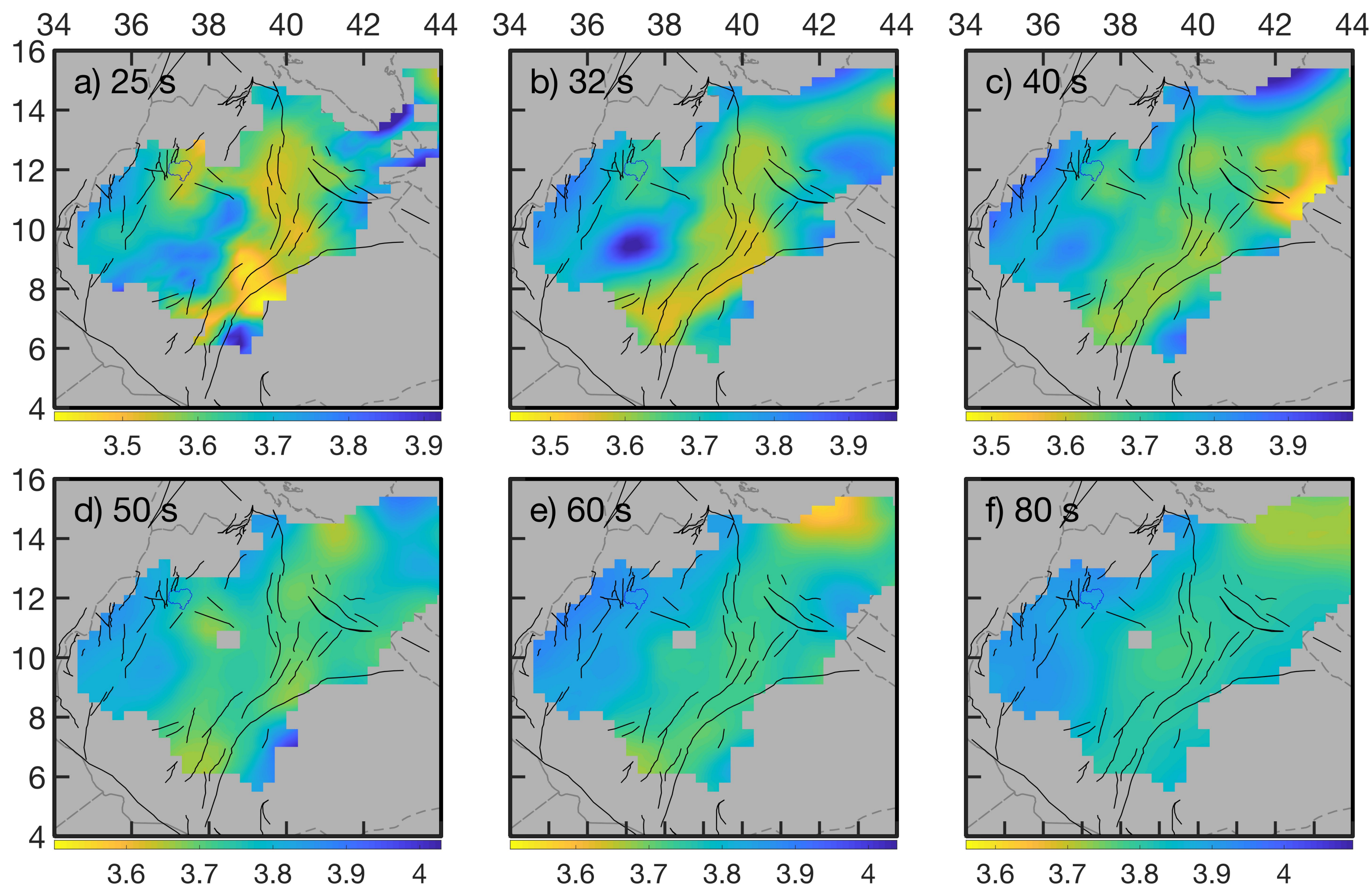

Figure 4: Phase velocities at 25, 32, 40, 50, 60 and 80 s from stacking of 5741 individual earthquake phase velocity maps, in km/s. Warmer colors indicate slower phase velocities; note change in color bounds with period. Lake Tana is plotted in blue, and faults from figure 1b) are plotted at each period.

4.3 Joint inversion

We inverted for shear velocity models at 28 station locations within the EP, NWEP, and MER. Stations in the CMER and SMER serve as points of comparison between our results and previous studies. We define data fit as the root mean square (RMS) data misfit, normalized by the RMS of the observed data. If the predicted data are identical to the observed, the misfit is zero, and data fit is 100%. If the predicted data are unrelated to the observed data, the data fit is 0%. Our mean data fit for phase velocities and RFs is 99.5% and 71.0%, respectively. This indicates that the inversion was able to more closely fit the smooth phase velocity curves than RFs.

4.3.1 Crustal Thickness

We report the median and 1σ (actually the $\pm 37^{th}$ percentile of the posterior ensemble about the median) crustal thicknesses at inverted stations (fig. 5a). Crustal thicknesses are similar to those found from the H-κ stacking method (SI fig. 1), but notable divergences appear at two stations in the central EP, indicating that phase velocities are not straightforwardly compatible with the receiver function constraints here.

The crust is thickest northeast of the central EP, and near Lake Tana, varying from 35 - 40 km. Stations in the CMER and Somalian plateau also exhibit thick crust of ∼37.5 km and ∼36.5 km, respectively. Crust at stations in the SMER is thinner, at ∼29 - 31 km. Trending northwest of the SMER axis to the central EP are three stations of similar thickness, ∼31 km, amongst ∼34 - 36 km thick crust.

Crustal thickness is bimodal along the slow phase velocity lineament, split between ∼29 - 30 km and ∼33 - 34 km. Crust in the NWEP is between 28.5 - 31 km. We find that our crustal thicknesses are more similar to those of Keranen et al. (2009) than Dugda et al. (2007) and Stuart et al. (2006), perhaps due to parameterization differences, but are not strongly inconsistent with the latter studies. A list of crustal thicknesses with associated standard deviation may be found in the supplement (T1).

4.3.2 Shear Velocities

We obtain a median shear velocity profile at each station from the posterior model ensemble. We focus on the velocities from 30 and 140 km depth due to the period range of our phase velocities. We display depth slices at 30, 50, 70 and 110 km (fig. 5b-e), and note that at 30 km the observed shear velocities represent crustal structure at most stations (fig. 5a). The 1σ shear velocity uncertainties between 60 and 120 km are approximately ± 0.05 km/s across all inverted stations. We compare stations' shear velocity profiles to a regional average and also to PREM (Dziewonski & Anderson, 1981), since we find that the entire region is substantially slower than a global average.

Shear velocities closely mirror the trends seen in phase velocities (fig. 4). Slow shear velocities exist in the CMER, SMER, and near-rift EP stations, but also near Lake Tana, and southeast of it along the EP. Fast velocities are resolved within the central EP, Somalian Plateau, and NWEP.

In the group 1 velocity aggregate (see section 3.5, figs. 5a, 1a), which spans the central EP, Somalian Plateau, and NWEP, we find shear velocities that are faster than the regional average at all depths. Group 1 shear velocities are 3.0 - 4.3% (0.13 - 0.19 km/s) slower than PREM from 60 - 120 km (fig. 6a, d), the range of depths most representative of shallow mantle structure that are most consistently resolved in our inversion (measured by similarity of shear velocity profiles within each group; fig. 6).

Four of six northwestern-most NWEP stations are faster than the regional average at 50 km by 1.2 - 4.8% (4.3 - 4.45 km/s). At 70 km depth and below, all six northwestern stations are 0.5 - 5% faster (4.27 - 4.46 km/s) than regional average (fig. 5d, e). Stations within the central EP manifest heterogeneous mean shear velocities between 30 and 50 km, but this region is 0 - 4% faster (4.25 - 4.42 km/s) than the regional average deeper than 50 km. The Somalian Plateau is faster than the regional average between 50 - 100 km by 1 - 3.5% (4.3 - 4.4 km/s).

At depths greater than $\sim$80 km, the group 1 shear velocity decreases gradually with depth ($\sim$0.0012 km/s per kilometer) instead of increasing, as is usually the case at this depth within the continents (*e.g.*, French & Romanowicz, 2014). This negative velocity gradient appears to represent a gradual base of the plate beneath a fast lithospheric lid.

Group 2 shear velocities, which include Lake Tana and EP stations to the southwest of it, display slower velocities than those found in group 1. Shear velocities are 4.6 - 6.2% (0.21 - 0.28 km/s) slower than PREM from 60 - 120 km (fig. 6b, d). Unlike group 1, group 2 velocity profiles seem to have a thin or absent lid, and actually get faster monotonically with depth; at depths greater than ∼100 km, they are statistically indistinguishable from group 1.

By 50 km, shear velocities in the southwestern EP and near Lake are moderately slower than the regional average by 0 - 2% (4.17 - 4.25 km/s), and remain so at 70 km (fig. 5c, d). By 110 km, only the southwestern EP shows reduced shear velocities slower than the regional average by 0 - 1% (4.2 - 4.25 km/s), while other stations throughout the EP are homogeneously faster than the regional average by 0.5 - 1.5% (4.27 - 4.31 km/s).

Group 3 shear velocities, which include the MER and the near-rift EPL, are the most reduced compared to PREM; 7.7 - 8.7% (0.34 - 0.39 km/s) slower from 60 - 120 km (fig. 6c, d). Between 50 and 110 km depth, these stations are slower than the regional average by 2 - 6% (4.00 - 4.17 km/s), with SMER stations displaying the slowest velocities. Station MERT displays an increase in shear velocity between ∼40 - 50 km, and then decreases between ∼50 - 60 km. This may be evidence of a thin fast lithospheric lid, which is not displayed by other stations in group 3.

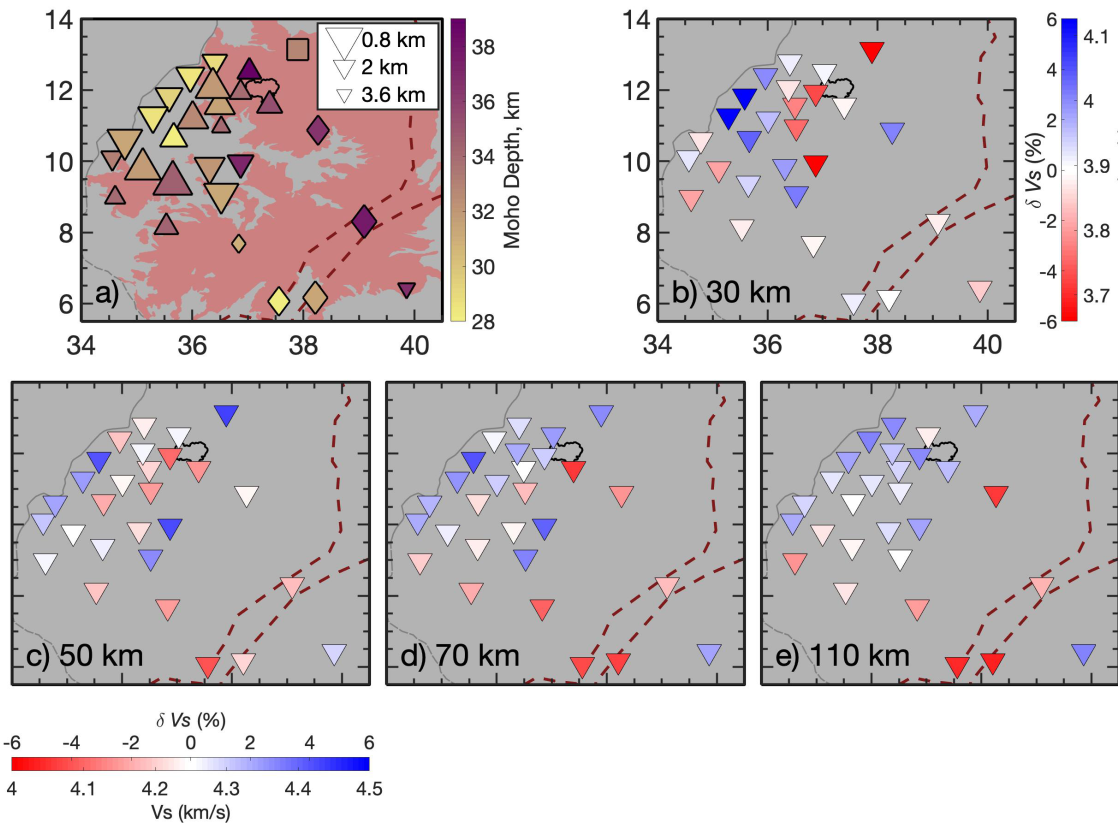

Figure 5: a) Post-inversion crustal thickness. Yellower colors indicate thinner crust, redder colors indicate thicker crust. Symbol size is scaled by $1/\sigma$ of the Moho depth from the posterior. Symbol type indicates velocity group, where group 1 = inverted triangle, group 2 = triangle, group 3 = diamond. Station DAQU is not grouped, and marked as a square. Flood basalt bounds are plotted in light red. b) - e) Median shear velocity from posterior ensembles of inverted stations at 30 (b), 50 (c), 70 (d) and 110 (e) km depth. Color signifies shear velocity scaled roughly by deviation from the mean velocity at each depth $\pm$ 6%. Velocities at 50, 70, and 110 km share the same color scaling, seen beneath subplot (c). On all subplots, the rough bounds of the MER rift valley are dashed in thick dark red, and Lake Tana in black.

5 Discussion

5.1 Regional Shear Velocity Trends

We find that mantle shear velocities are slower than PREM for all stations and velocity aggregate groups, even the "fast" group 1 (fig. 6d). These reduced shear velocities point to systematically elevated temperature from a regionally pervasive source (Dugda et al., 2007), a more silicic mantle composition, grain size reduction, the presence of melt and other fluids, or a combination of these factors (Faul & Jackson, 2005).

In the Central EP, Somalian Plateau, and NWEP (group 1), we find a fast velocity lithospheric lid between ∼40 - 80 km depth. In our mean shear velocity profiles, constrained primarily by phase velocities, this feature appears to grade gradually with depth into lower velocities, implying a gradual lithosphere-asthenosphere boundary. However, at some of the stations in this region RFs also record a negative shear velocity gradient, seen in others' work (Lavayssière et al., 2018).

A fast lithospheric lid is also present in the Mozambique Belt (Weeraratne et al., 2003) between the Moho and ∼60 - 80 km depth. We argue that the Mozambique Belt represents an informative reference structure because of the belt's continuous nature along Eastern Africa (Keranen et al., 2009; Meert & Lieberman, 2008), with subsequent velocity differences being a result of plume impingement and associated volcanism.

The similarity in shear velocity structure, but uniformly slower velocities of group 1 compared to the Mozambique Belt, suggest holistic velocity perturbations from the original lithospheric structure far off-rift (fig. 6a, d). At ∼45 km depth, the group 1 profile is ∼0.25 km/s slower than the Mozambique Belt. Velocities in the two regions gradually become more similar with depth, and are barely distinguishable by ∼165 km. The fact that these regions seem to differ particularly in shallow mantle structure suggests that reduced shear velocities in the Ethiopian plateau extend well up into the lithosphere.

Middling shear velocities in group 2 are distinct from group 1 and 3, with stations in this region lacking a fast velocity lid, but also failing to display a negative concave velocity structure between 40 - 140 km (fig. 6b, d). Shear velocities are maximally ∼3.5%, or 0.13 km/s slower than group 1, but faster than group 3 by a maximum of ∼3.8%, or 0.15 km/s. We interpret this region as manifesting an intermediate rifting state between two end-members (the far flank and the MER). We do note that shear velocities within group 2 are more heterogeneous than groups 1 and 3, a reflection of complex crustal structure. Dugda et al. (2007) observed a lack of a fast velocity lid in the MER and Afar, and concluded that advanced thermal erosion of the lithosphere had already taken place within the rift [*cf.* Rychert et al. (2012)]. We similarly propose that the lack of a fast velocity lid within the EP slow velocity lineament is indicative of substantial rift-associated thermal lithospheric erosion surprisingly far from the rift axis (see section 5.3).

Slow shear velocities in the MER and nearby EP support extensive upper mantle modification, consistent with the tectonic and thermal effects of rifting. For reference, we compare group 3 to the mean global shear velocity structure of 0 - 25 Ma oceanic crust from the compilation of French et al. (2013) and find $V_S(z)$ is slower than this reference by 3.6 - 4.3% (fig. 6c, d). The fact that these values are even slower than the young oceans likely reflects unusually high mantle potential temperatures and/or less mature melt percolation network beneath still-extant continental crust, as well as perhaps a high-biasing of the oceanic regional average by cooler off-ridge structure. Taken at face value, and ignoring temperature differences, the ∼4% offset reflects an excess of between 0.5% and 4% *in situ* melt compared to the young oceans depending on the chosen scaling (MELT Seismic Team, 1998; Faul et al., 1994; W. C. Hammond & Humphreys, 2000). The similarity in velocity profile shape is evidence that the maturation of the rifted asthenosphere significantly precedes crustal breakup here (Keranen et al., 2009; Eilon et al., 2015).

5.2 Physical Interpretation of Low Velocities

We observe low velocities throughout the EP, NWEP, and Somalian Plateau. Compositional variance between pyrolite, piclogite, and harzburgite can account for only ∼1% δVs (Cammarano et al., 2003), and grain size reduction from 1 cm to 1 mm at 1200 °C reduces velocities a maximum of 0.1 km/s (Hirth & Kohlstedf, 2003), or ∼2% δVs (Keranen et al., 2009). Our data therefore strongly support the presence of elevated mantle temperatures and/or *in situ* melt fraction

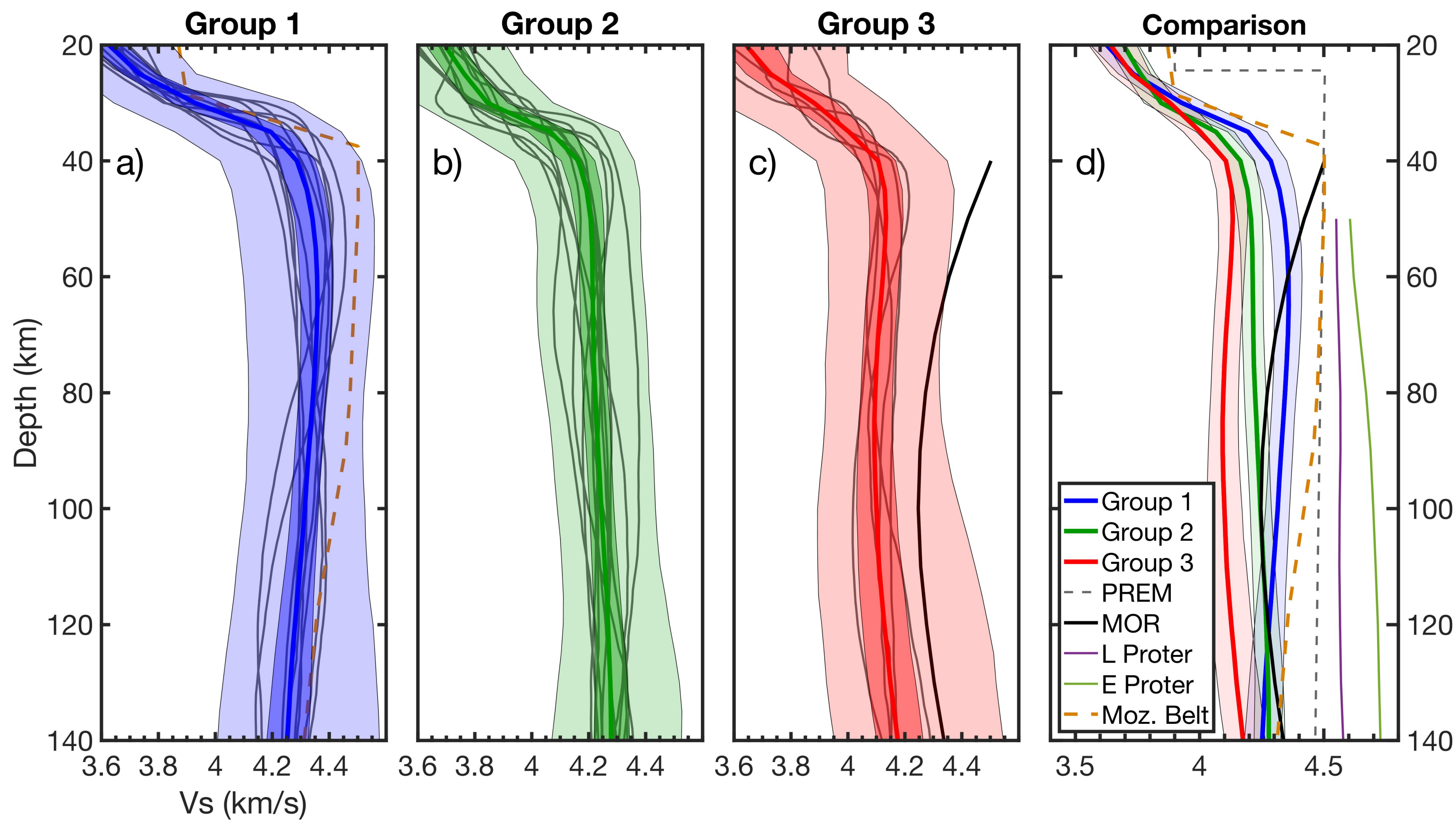

Figure 6: Grouped shear velocity profiles for all stations jointly inverted. a,b,c) show groups 1, 2, and 3, respectively, where light grey lines are individual median Vs profiles of the aggregated stations. The median group Vs profile is shown in thick colored lines, while dark and light shaded patches correspond to 1σ and 2σ bounds developed by combining model posteriors for all stations in the group. d) compares the median $\pm 1\sigma$ profiles of all groups together with reference models including 0 - 25 Ma mid ocean ridge (black), late Proterozoic crust (purple), and early Proterozoic crust (light green) (French et al., 2013), the Mozambique Belt (dashed orange) (Weeraratne et al., 2003), and PREM (Dziewonski & Anderson, 1981). The Mozambique belt and 0 - 25 Ma mid ocean ridge profiles are also plotted on panels a) and c), respectively.

throughout this focus region. Dugda et al. (2007) reconciled slow MER shear velocities with the $\sim$0.3 km/s faster Mozambique Belt by invoking instantaneous thinning of the lithosphere from impingement of the Afar plume $\sim$30 Ma, with an associated $\sim$250 °C temperature increase. Other tomographic studies posit even hotter temperatures, up to 550 °C more than normal mantle temperatures (Chambers et al., 2019), to explain observed velocities.

We attempt to quantitatively connect our shear velocity observations to mantle conditions in two ways. First, by generating a suite of geotherms and forward-modelling shear velocity profiles, seeking a best fit to the average Vs(z) of each group. Candidate geotherms are constructed by grid searching over a range of mantle potential temperatures (T_p), surface heat flows (q_0), and radiogenic crustal heat production values (A_0) (figs. S5 - S7). We use the formulation of Takei (2017) to compute $V_S(T, z, d)$ at 1 Hz. We assume a grain size, d, of 1 mm, obtain anharmonic shear moduli from the tool of (Abers & Hacker, 2016) assuming a pyrolitic composition, and calculating self-consistent pressure profiles. Continental geotherms cannot fully predict observed shear velocities between 30 and 60 km (figs. S2-S4) using existing scaling relationships (Dalton & Faul, 2010), so we choose to minimize predicted misfit between 60 and 120 km, the range where our phase velocities are most sensitive, and the majority of melt is expected to reside.

We augment our velocity forward calculation to account for the velocity reduction effects of partial melt. We use super-solidus temperature excess to predict a melt fraction, assuming 0.0995% melt is generated per degree Celsius above the dry peridotite solidus (fig. 7a), which was calculated from a pMELTS algorithm curve (Ghiorso et al., 2002) using a LOSIMG composition peridotite (Hart & Zindler, 1986), at 3 GPa with no melt escape. We translate this melt fraction into a velocity reduction beyond the melt-free case using the relationship from Faul et al. (1994), whereby 1% partial melt slows shear velocities by 3.3%. We account for melt percolation effects by convolving the instantaneous melt curve with an exponential function to smooth melt upwards with decay lengthscale of 20 km. We also apply a compaction function downwards at the Moho with a lengthscale of 5 km to mimic the effect of neutral buoyancy of the mafic melt in the crust while ensuring total melt percentage is preserved. This procedure is admittedly *ad hoc*, and acts to distribute the effect of any melt across a broader depth range, in keeping with our lack of observed sharp low velocity layers. A second caveat is that we are combining a melt-free anelastic scaling law with a nominally anharmonic constitutive relationship for the effect of melt on velocity. However, given the absence of a more self-consistent approach and the other uncertainties in this forward modelling approach, we argue that this is a good approximation to balancing the effects of temperature and melt on velocity.

Second, we take a simpler approach, positing that independent effects of excess temperature (dT) and *in situ* melt fraction (ϕ) can explain slowness compared to PREM (δV_S), at some representative depth. We assume that $\delta V_S = \frac{\partial V_S}{\partial T}\delta T + \frac{\partial V_S}{\partial \phi}\delta\phi$, using derivatives of -0.0012 km/s/K (Dugda et al., 2007; Faul & Jackson, 2005; Jackson et al., 2002) and -0.047 km/s/% (Faul et al., 1994), respectively. Note that we prefer this model to W. C. Hammond and Humphreys (2000) as it provides an upper bound for melt percentage. Consistent with method 1, we use average the Vs between 60 - 120 km for each group (4.33 $\pm$ 0.053 km/s for group 1, 4.25 $\pm$ 0.048 km/s for group 2, and 4.11 $\pm$ 0.063 km/s for group 3) to yield contours of relative slowness for each group in reference to PREM (4.47 km/s Voigt average) (fig. 7b). We assume that PREM represents a melt-free mantle with a potential temperature of 1300 °C, and account for a 0.4 K/km adiabat when extending to 90 km depth. Naively, this approach is limited to establishing the linear trade-off between thermal and melt perturbations. However, these parameters are themselves of course linked. We therefore use the pMELTS calculation described above to compute the peridotite melting curve (fig. 7b) at 3 GPa (~90 km depth). Theoretically, the intersection between this curve and the groups' slowness contours constrains mantle conditions.

Using method 1, group 1 is best fit by a geotherm with parameters: 45 km Moho, Q_0 = 75 mW/m^2, T_p = 1425°C, A_0 = 0.99e^{-7} W/m^3. This estimate agrees with independent xenolith-based estimates of local mantle temperatures in the range 1350 - 1450 °C (Rooney et al., 2012; Armitage et al., 2015) within the MER and Afar. This geotherm does not intersect the solidus of dry peridotite - high temperatures alone are sufficient to explain these velocities (fig. 7a). Similarly, the PREM-comparison method 2 suggests an upper mantle temperature ~100°C above average. According to our assumptions, this curve does not intersect the pMELTS melting curve (fig. 7b); the models do not seem to require *in situ* melt here.

This is in agreement with an absence of volcanism in the NWEP. While some thermal springs exist near the central EP, no recent volcanism exists in any location aggregated into group 1. Group 1 stations sit atop the coolest mantle in the region, apparently ∼1450°. ∼30 Ma xenolith geothermobarometry near Injabara (Ferrando et al., 2008) (fig. 7a) and potential temperature estimates of 1410°C from primitive magmas 10 - 40 Ma (Rooney et al., 2012) imply that in the past ambient mantle temperatures were lower than those recorded today for group 1. Thus, even in the distal flank of the rift, there seems to be a warming trend over time.

Group 2 is best fit by a geotherm with parameters: 30 km Moho, $Q_0 = 75$ mW/m^2, $T_p =$ 1475°C, $A_0 = 1.32e^{-6}$ W/m^3. This is hotter than the 1350 - 1450 °C ambient mantle temperatures estimated for the MER and Afar (Rooney et al., 2012; Armitage et al., 2015). Group 2 velocity averages are low enough to require the presence of upper mantle partial melt. A maximum of 0.46% partial melt is found at 70 km depth (fig. 7a) using method 1, while the range in δVs of 4.6% (0.21 km/s) and 5.8% (0.26 km/s) correspond to 0.6 - 0.74% melt using the second method. The second method predicts a mantle temperature of 1500 °C, and 0.1% melt (fig. 7b). This 0.1 - 0.74% partial melt component is slightly lower than the 1.1% melt component required by Chambers et al. (2019) to the east of Lake Tana, possibly because here we group the slower northern and less slow southern stations in the off-axis lineament.

Xenolith data from Conticelli et al. (1999); Ferrando et al. (2008) at Injibara, a region just south of Lake Tana, contain signatures of hydrous enrichment. Xenoliths indicate the mantle here is primarily depleted peridotite (Conticelli et al., 1999; Rooney et al., 2012) which may require hydration for substantial melt absent very high temperatures (Asimow et al., 2004). Quaternary volcanoes and thermal springs clustered south of Lake Tana lie within a region of reduced phase and shear velocities, while thermal springs trending east of Lake Tana follow surficial border faults and have been linked to shallow velocity reduction (Korostelev et al., 2015; Chambers et al., 2019). These features support hydration and melt near Lake Tana. These surface features extend southwest from Lake Tana as far as 11°N. Our results provide evidence for elevated temperature and likely melt that extend even further southwest, to 10°N or even further south; if this slow lineament represents southward migration of extension then the shallow expression of off-rift tectonism seems to be lagging the imaged perturbation at depth.

Group 3 is best fit by a geotherm with parameters: 30 km Moho, $Q_0 = 75$ mW/m^2, $T_p =$ 1525 °C, $A_0 = 1.65e^{-6}$ W/m^3. This is hotter than the proposed 1350 - 1450 °C mantle temperature from geochemical constraints (Rooney et al., 2012; Armitage et al., 2015) by 75 - 175 °C, requiring a melt component. A maximum of 1% partial melt at 80 km (fig. 7a) is expected using the first method. δVs of 7.2% (0.32 km/s) and 8.8% (0.40 km/s) correspond to 0.9 - 1.1% melt between 60 and 120 km using the first method. The second method predicts a mantle temperature of 1515 °C, and 0.95% melt (fig. 7b). These methods closely agree on a partial melt percentage $\sim$1%, which aligns with recent estimates within the MER between 0.5 - 10% (Keranen et al., 2009; Guidarelli et al., 2011; Gallacher et al., 2016; Chambers et al., 2019). The presence of abundant melt at depth associated with the MER is consistent with abundant surface volcanism and previous work (White & McKenzie, 1995; Armitage et al., 2010; J. O. Hammond, 2014). It is interesting to note that while volcanoes are confined mostly to the narrow rift valley (fig. 1b), our phase velocities are slow in a relatively broad swath extending 100 km beyond the border faults even at 32 - 40 s. This contrast may stem partly from resolution issues, but likely also reflects the nature of melt channelization and focusing within the rift [*cf.* (Holtzman & Kendall, 2010)].

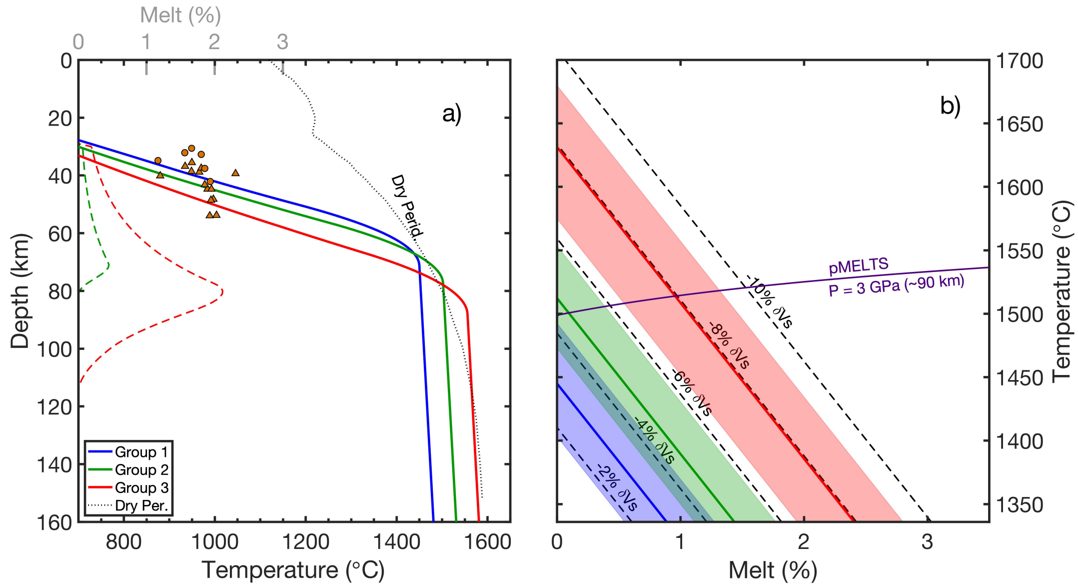

Figure 7: a) Best fit geotherms for group 1 (blue), group 2 (green), and group 3 (red) using method 1 to fit shear velocity between 60-120 km depth (Section 5.2), with temperatures indicated by the lower x-axis. The dry peridotite solidus from Asimow et al. (2004) is plotted in black dots. Xenolith pressure - temperature equilibration conditions from Conticelli et al. (1999) and Ferrando et al. (2008) are shown in orange circles and triangles, respectively. Partial melt percent (upper x-axis) calculated using the super-solidus forward modeling method is shown for groups 2 and 3 (dashed, colored as above) to the left. b) The slowness domain, showing linear tradeoff between melt and mantle temperature excess, contoured in increments of -2% δVs. Mean $\pm 1\sigma$ slowness compared to PREM between depths of 60-120 km is shown for each velocity group (colors as above). The melting curve of a LOSIMG composition peridotite (Hart & Zindler, 1986) at 3 Gpa is plotted in solid purple.

5.3 Crustal Thickness Variations

The Moho depths we observe in the center of the Ethiopian Plateau are qualitatively consistent with crustal thickening following the impingement of the Afar Plume ~30 Ma (Mackenzie et al., 2005; Stuart et al., 2006). This event is thought to have thickened the crust in two ways:

up 2 km of flood basalt emplacement at the surface (Baker et al., 1996; Hofmann et al., 1997; Ukstins et al., 2002), accompanied by up to 10 km of underplating, yielding a total crustal thickness up to ∼45 km. This is best observed from wide-angle seismic reflection/refraction data (Mackenzie et al., 2005), but that study only imaged the deepest crust ∼100 km on either side of the rift valley. Some degree of thickening by igneous intrusion is also well recorded by gravity surveys (Cornwell et al., 2006), and increased Vp/Vs ratios signifying a more mafic crustal composition (Ogden et al., 2019). Xenolith data collected along the YTVL also support underplated material beneath the near-rift EP (Abebe et al., 1998; Adhana, 2014; Rooney et al., 2017), and melt emplacement well outside the rift axis is supported by abundant silicic and basaltic dikes (Mège & Korme, 2004) west of Lake Tana, where magmatism exploited zones of pre-existing weakness.

We do not observe crust as thick as 45 km in our field region. The average crustal thickness of stations in our inversion within the EP is 34 km, and the thickest crust we see is 39 km at SERE, just north of Lake Tana. Ignoring erosion, 12 km of thickening would suggest a pre-plume thickness of 22 km in the plateau, which we argue is unrealistically thin for continental crust. In order to estimate an appropriate baseline, we propose that stations that lie outside the bounds of flood basalt emplacement (fig. 1b) in the NW of our field region exemplify pre-rift/plume lithospheric structure and crustal thickness: ∼30 - 32 km (fig. 5). One caveat is that four of six of these stations lie within the erosional basin of the Blue Nile Gorge, which has incised a mean of 0.37 km of rock within the basin since 29 Ma (Gani et al., 2007). As another regional comparison, ∼35 km crust is observed further west in Sudan (El Tahir et al., 2013; Mohamed et al., 2001), which similarly lacks flood basalts or underplating.

With this baseline of ∼31 km, the crustal thicknesses of 31-39 km we see in the EP to Lake Tana imply igneous addition on the order of 0 - 8 km, distributed non-uniformly across the region. This disparity in estimated underplating compared to previous studies may simply be geographical - there was more igneous thickening in the region of the MER than on the flank. Alternatively, it might be methodological; our receiver functions might be sensing the substantial velocity boundary between pre-existing crust and igneous underplate, and not the (perhaps more gradational) underplate-mantle boundary (Stuart et al., 2006) to which wide-angle reflection/refraction is more suited. Nonetheless, since our method attempts to fit the full receiver function waveform, and since we do not see an abundance of double-peaked Pxs phases, we estimate that the crustal thickness patterns we see are real.

Two observations stand out in the EP slow velocity lineament: Firstly the thickest crust in our field region is around Lake Tana and coincides with some of the lowest off-rift shear/phase velocities. Secondly, we see a modest trend of thinning to the southwest (fig. 5a). This tapering has several possible explanations. It may be that more erosion has occurred in the south-central plateau than previously thought, or alternatively that plume emplaced more igneous material to the north. Finally, it may be that the pre-plume, pre-extension thickness increased from north to south; N-S trending sutures are more concentrated near Lake Tana (fig. 1b) perhaps connoting more compressional strain in that area in the geologic past. This region is further discussed in Section 5.4.

Although we only include three stations from within the rift axis in this study, they show evidence for thin crust within the SMER (<31 km), and thicker crust (∼38 km) within the CMER, consistent with previous work (Keranen et al., 2009; Stuart et al., 2006; Dugda et al., 2007). Although simple models of pure shear rifting would predict the thinnest crust in the region within the well defined rift valley (Buck, 1991), thicker crust in the CMER supports complex, diachronous rift evolution of the MER (Wolfenden et al., 2004; Bonini et al., 2005; Keranen & Klemperer, 2008).

5.4 Off - Axis Extension

Reduced shear velocities along a rift-parallel lineament extending south west from Lake Tana are the strongest evidence to date of off-axis extension within the study region. The northern portion of the slow lineament coincides with Quaternary volcanoes, spatter cones, fumaroles, and thermal springs (fig. 1b) (Abebe et al., 1998; Kieffer et al., 2004; Keir et al., 2009). These are concentrated near Lake Tana, where we find the slowest velocities, and where calculations (Section 5.2) seem to require 0.1 - 0.74% partial melt in the upper mantle to fit group 2 Vs observations. This region is also observed to have regionally pervasive slow P and S-wave arrivals (Bastow et al., 2005, 2008; Keir et al., 2009; Boyce et al., 2021) and small amounts (< 1mm/yr) of contemporary surface extension as determined by GPS measurements(Birhanu et al., 2016). We attribute this collection of evidence to localised, shallow extension >450 km from the rift axis.

Shear velocities and surficial features agree that the northern portion of the slow velocity lineament is more mature than the southern, which is also supported by a higher degree of magmatism and larger magnitude GPS velocity measurements near the south of Lake Tana (fig. 1a). N-S trending sutures, that accommodated the crustal shortening from East and West Gondwana colliding (Shackleton, 1986) and were later deformed by E-W shortening and transpressive shear (Johnson et al., 2004), may remain active zones of weakness, accommodating extension in the West Ethiopian Shield too shallow to be observed by our methods, or sparse geodetic coverage.

As noted above, it is interesting that notably thick crust near Lake Tana (~36 - 39 km) coincides with some of the slowest upper mantle velocities (Figure 5). Moreover, stations in group 2 which correspond to the low velocity lineament, have average – or deeper than average – Moho depths. The combination of both low shear velocities and only moderate crustal thickening within EP is, at face value, paradoxical. We propose two potential explanations in the context of off-axis extension. One possibility is that >10 km of magmatically driven thickening (Mackenzie et al., 2005) associated with plume impingement has taken place, following which high (>40%) strain pure shear extension in the plateau - evidenced by slow shear velocities - has re-thinned the crust by up to 9 km to present day values (~30 - 39 km). Alternatively, extension off axis has reduced velocities due to lithospheric degradation (Havlin et al., 2013) and melt percolation, but is still too immature to have initiated much crustal thinning. In this case, our results would seem to be inconsistent with >5km of magmatic thickening. It may be that underplating of the Ethiopian plateau tapers substantially away from the - now rifted - center. The more parsimonious explanation would seem to be the latter; melt and thermal effects of incipient rifting well precede crustal breakup, at least within Ethiopia.

P- and S-wave delay time observations and tomography of the Ethiopian plateau have previously hinted at slow upper mantle extending well beyond the MER valley (Bastow et al., 2005, 2008; Keir et al., 2009). Absolute P-wave delay times of up to 1 second imply δV_p of as more than -2% off axis, with these low velocities asymmetrically observed to the north west of the rift (Boyce et al., 2021). These results agree qualitatively with our data, which reveal upper mantle velocities 4.3% (0.19 km/s) slower than PREM in the group 2 region. Clearly, there is substantial thermal perturbation and -our calculations imply- *in situ* melt beneath large swaths of the Ethiopian plateau, with particular apparent concentration in the slow velocity lineament.

Geodetic data suggest that while the majority of extension in the northern EARS is localized within the MER and Afar, up to ∼20%, or 1 - 2 mm/yr, of extension may be distributed across the EP (Birhanu et al., 2016). Keranen et al. (2009) have interpreted crustal thickness maps as implying broad distribution of strain beyond the MER. Small magnitude GPS measurements in the EP of <1 mm/yr are of similar magnitude to those in the near-MER EP (fig. 1a) (Birhanu et al., 2016), suggesting extensional accommodation is present in both locales.

6 Conclusions

We have investigated the northwestern EP flank of the East African Rift and Ethiopian Plateau using Rayleigh wave phase velocity measurements and Ps receiver functions to interrogate the deep crustal and shallow mantle structure. We jointly inverted these data for shear velocity profiles using a trans-dimensional, hierarchical Bayesian inversion algorithm, incorporating H-κ receiver function stacks to constrain crustal thickness.

Throughout the study region we found slow phase and shear velocities, reflecting mantle temperatures significantly elevated compared to a stable continent. We showed that high temperatures and *in situ* mantle melt content extend out to the flanks of the rift. The central Ethiopian plateau has a fast lid above a gradual negative velocity gradient. Within and near the SMER, we found maximally thinned crust and extremely low upper mantle velocities - the effects of rifting are clear. Similarly thin crust within the NWEP flank, on the other hand, is paired with fast upper mantle velocities. These flank stations appear to be the best local representatives of prerift and pre-plume lithosphere, relatively unaffected by either process.

In the NWEP, we observed a lineament sub-parallel to the rift axis with slow shallow upper mantle velocities. This lineament coincides with GPS-observed divergence, pervasively delayed teleseismic arrivals, and Quaternary aged volcanism, fumaroles, and thermal springs near Lake Tana. These observations support the presence of localized off-axis extension, hundreds of kilometers from the MER. Plume-derived underplating and flood basalts cause ambiguity in determining the extensional maturity of the slow velocity lineament. If igneous addition has offset crustal thinning this region may already be heavily extended. Alternatively, there may be insufficient off-axis extension to have allowed much crustal thinning at all, but melt percolation and lithospheric degradation have already begun to substantially reduce shear velocity. In either case, it is apparent that some amount of that off-rift extension occurs well away from the MER, and that continental breakup in Ethiopia is more complex than simple narrow rifting.

Acknowledgments

This project was funded by NSF grant EAR-1723170. All data used are available through Iris Data Management Center (https://ds.iris.edu). Supplementary data are available in the supplementary figures document, and as a zip file. The authors know of no real or perceived financial or affiliatory conflicts of interest. Special thanks to Ge Jin and Natalie Accardo for help in clarifying ASWMS procedures, and Katie Keranen for providing insight into the project.

Data Availability Statement All data used are available from the Iris Data Management Center (`https://service.iris.edu/`). IRIS Data Services are funded through the Seismological Facilities for the Advancement of Geoscience (SAGE) Award of the National Science Foundation under Cooperative Support Agreement EAR-1851048 and EAR-1261681. Networks used to develop Rayleigh wave phase velocity maps and receiver functions, in alphabetical order, are: AFAR0911 2H (`https://doi.org/10.7914/SN/2H_2009`), NABRO 4H (`https://doi.org/10.7914/SN/4H_2011`), ESP 5H (`https://doi.org/10.7914/SN/5H_2011`), AfricaArray AF (`https://doi.org/10.7914/SN/AF`), GEOSCOPE G (`https://doi.org/10.18715/GEOSCOPE.G`), GSN IU (`https://doi.org/10.7914/SN/IU`), XI (`https://doi.org/10.7914/SN/XI_2000`), EAGLE II XJ (`https://www.fdsn.org/networks/detail/XJ_2002/`), ARGOS XM (`https://doi.org/10.7914/SN/XM_2012`), YOCMAL XW (`https://doi.org/10.7914/SN/XW_2009`), Riftvolc Y6 (`https://doi.org/10.7914/SN/Y6`

_2016), EAGLE YJ (https://www.fdsn.org/networks/detail/YJ_2001), Ethiopia YY (https://doi.org/10.7914/SN/YY_2013), Boina YZ (https://www.fdsn.org/networks/detail/YZ_2005/), OldAFAR ZE (https://doi.org/10.7914/SN/ZE_2007), AFAR ZF (http://www.fdsn.org/networks/detail/ZF_2007/), ADDSA ZK (https://doi.org/10.7914/SN/ZK_2009).

References

Abate, B., Koeberl, C., Buchanan, P. C., & Körner, W. (1998). Petrography and geochemistry of basaltic and rhyodacitic rocks from lake tana and the gimjabet-kosober areas (north central ethiopia). *Journal of African Earth Sciences*, *26*(1), 119–134.

Abebe, T., Mazzarini, F., Innocenti, F., & Manetti, P. (1998). The yerer-tullu wellel volcanotectonic lineament: A transtensional structure in central ethiopia and the associated magmatic activity. *Journal of African Earth Sciences*, *26*(1), 135–150.

Abers, G. A., & Hacker, B. R. (2016). A matlab toolbox and e xcel workbook for calculating the densities, seismic wave speeds, and major element composition of minerals and rocks at pressure and temperature. *Geochemistry, Geophysics, Geosystems*, *17*(2), 616–624.

Abt, D. L., Fischer, K., French, S., Ford, H., Yuan, H., & Romanowicz, B. (2010). North american lithospheric discontinuity structure imaged by ps and sp receiver functions. *Journal of Geophysical Research*, *115*, 1-24.

Adhana, T. A. (2014). The occurrence of a complete continental rift type of volcanic rocks suite along the yerer–tullu wellel volcano tectonic lineament, central ethiopia. *Journal of African Earth Sciences*, *99*, 374–385.

Armitage, J. J., Collier, J. S., & Minshull, T. A. (2010). The importance of rift history for volcanic margin formation. *Nature*, *465*(7300), 913–917.

Armitage, J. J., Ferguson, D. J., Goes, S., Hammond, J. O., Calais, E., Rychert, C. A., & Harmon, N. (2015). Upper mantle temperature and the onset of extension and break-up in afar, africa. *Earth and Planetary Science Letters*, *418*, 78–90.

Asimow, P. D., Dixon, J. E., & Langmuir, C. (2004). A hydrous melting and fractionation model for mid-ocean ridge basalts: Application to the mid-atlantic ridge near the azores. *Geochemistry, Geophysics, Geosystems*, *5*(1).

Baker, J., Snee, L., & Menzies, M. (1996). A brief oligocene period of flood volcanism in yemen: implications for the duration and rate of continental flood volcanism at the afro-arabian triple junction. *Earth and Planetary Science Letters*, *138*(1-4), 39–55.

Bastow, I. D., Nyblade, A., Stuart, G., Rooney, T., & Benoit, M. (2008). Upper mantle seismic structure beneath the ethiopian hot spot: Rifting at the edge of the african low-velocity anomaly. *Geochemistry, Geophysics, Geosystems*, *9*(12).

Bastow, I. D., Stuart, G. W., Kendall, J.-M., & Ebinger, C. J. (2005). Upper-mantle seismic structure in a region of incipient continental breakup: northern ethiopian rift. *Geophysical Journal International*, *162*(2), 479–493.

Benoit, M. H., Nyblade, A. A., & VanDecar, J. C. (2006). Upper mantle p-wave speed variations beneath ethiopia and the origin of the afar hotspot. *Geology*, *34*(5), 329–332.

Berhe, S. M. (1990). Ophiolites in northeast and east africa: implications for proterozoic crustal growth. *Journal of the Geological Society*, *147*(1), 41–57.

Birhanu, Y., Bendick, R., Fisseha, S., Lewi, E., Floyd, M., King, R., & Reilinger, R. (2016). Gps constraints on broad scale extension in the ethiopian highlands and main ethiopian rift. *Geophysical Research Letters*, *43*(13), 6844–6851.

Bodin, T., Leiva, J., Romanowicz, B., Maupin, V., & Yuan, H. (2016). Imaging anisotropic layering with bayesian inversion of multiple data types. *Geophysical Journal International*, *206*(1), 605–629.

Bodin, T., Yuan, H., & Romanowicz, B. (2014). Inversion of receiver functions without deconvolution—application to the indian craton. *Geophysical Journal International*, *196*(2), 1025–1033.

Bonini, M., Corti, G., Innocenti, F., Manetti, P., Mazzarini, F., Abebe, T., & Pecskay, Z. (2005). Evolution of the main ethiopian rift in the frame of afar and kenya rifts propagation. *Tectonics*, *24*(1).

Boyce, A., Bastow, I. D., Cottaar, S., Kounoudis, R., Guilloud De Courbeville, J., Caunt, E., & Desai, S. (2021). Afrp20: New p-wavespeed model for the african mantle reveals two whole-mantle plumes below east africa and neoproterozoic modification of the tanzania craton. *Geochemistry, Geophysics, Geosystems*, *22*(3), e2020GC009302.

Buck, W. R. (1991). Modes of continental lithospheric extension. *Journal of Geophysical Research: Solid Earth*, *96*(B12), 20161–20178.

Burke, K., & Sengör, C. (1986). Tectonic escape in the evolution of the continental crust. *Reflection seismology: the continental crust*, *14*, 41–53.

Calò, M., Bodin, T., & Romanowicz, B. (2016). Layered structure in the upper mantle across north america from joint inversion of long and short period seismic data. *Earth and Planetary Science Letters*, *449*, 164–175.

Cammarano, F., Goes, S., Vacher, P., & Giardini, D. (2003). Inferring upper-mantle temperatures from seismic velocities. *Physics of the Earth and Planetary Interiors*, *138*(3-4), 197–222.

Chambers, E. L., Harmon, N., Keir, D., & Rychert, C. A. (2019). Using ambient noise to image the northern east african rift. *Geochemistry, Geophysics, Geosystems*, *20*(4), 2091–2109.

Chernet, T., Hart, W. K., Aronson, J. L., & Walter, R. C. (1998). New age constraints on the timing of volcanism and tectonism in the northern main ethiopian rift–southern afar transition zone (ethiopia). *Journal of Volcanology and Geothermal Research*, *80*(3-4), 267–280.

Conticelli, S., Sintoni, M., Abebe, T., Mazzarini, F., & Manetti, P. (1999). Petrology and geochemistry of ultramafic xenoliths and host lavas from the ethiopian volcanic province: An insight into the upper mantle under eastern africa. *Acta Vulcanologica*, *11*, 143–160.

Cornwell, D., Mackenzie, G., England, R., Maguire, P., Asfaw, L., & Oluma, B. (2006). Northern main ethiopian rift crustal structure from new high-precision gravity data. *Geological Society, London, Special Publications*, *259*(1), 307–321.

Corti, G. (2009). Continental rift evolution: from rift initiation to incipient break-up in the main ethiopian rift, east africa. *Earth-Science Reviews*, *96*(1-2), 1–53.

Dalton, C. A., & Faul, U. H. (2010). The oceanic and cratonic upper mantle: Clues from joint interpretation of global velocity and attenuation models. *Lithos*, *120*(1-2), 160–172.

Drilleau, M., Beucler, E., Mocquet, A., Verhoeven, O., Moebs, G., Burgos, G., ... Vacher, P. (2013). A bayesian approach to infer radial models of temperature and anisotropy in the transition zone from surface wave dispersion curves. *Geophysical Journal International*, *195*(2), 1165–1183.

Dugda, M. T., Nyblade, A. A., & Julia, J. (2007). Thin lithosphere beneath the ethiopian plateau revealed by a joint inversion of rayleigh wave group velocities and receiver functions. *Journal of Geophysical Research: Solid Earth*, *112*(B8).

Dziewonski, A. M., & Anderson, D. L. (1981). Preliminary reference earth model. *Physics of the earth and planetary interiors*, *25*(4), 297–356.

Ebinger, C., & Casey, M. (2001). Continental breakup in magmatic provinces: An ethiopian example. *Geology*, *29*(6), 527–530.

Ebinger, C., Yemane, T., Harding, D., Tesfaye, S., Kelley, S., & Rex, D. (2000). Rift deflection, migration, and propagation: Linkage of the ethiopian and eastern rifts, africa. *Geological Society of America Bulletin*, *112*(2), 163–176.

Ebinger, C. J., & Sleep, N. (1998). Cenozoic magmatism throughout east africa resulting from impact of a single plume. *Nature*, *395*(6704), 788–791.

Ebinger, C. J., Yemane, T., Woldegabriel, G., Aronson, J., & Walter, R. (1993). Late eocene–recent volcanism and faulting in the southern main ethiopian rift. *Journal of the Geological Society*, *150*(1), 99–108.

Eilon, Z., Abers, G. A., Gaherty, J. B., & Jin, G. (2015). Imaging continental breakup using teleseismic body waves: The w oodlark r ift, p apua n ew g uinea. *Geochemistry, Geophysics, Geosystems*, *16*(8), 2529–2548.

Eilon, Z., Fischer, K. M., & Dalton, C. A. (2018). An adaptive bayesian inversion for upper-mantle structure using surface waves and scattered body waves. *Geophysical Journal International*, *214*(1), 232–253.

El Tahir, N., Nyblade, A., Julià, J., & Durrheim, R. (2013). Crustal structure of the khartoum basin, sudan. *Tectonophysics*, *593*, 151–160.

Ester, M., Kriegel, H.-P., Sander, J., Xu, X., et al. (1996). A density-based algorithm for discovering clusters in large spatial databases with noise. In *Kdd* (Vol. 96, pp. 226–231).

Faul, U. H., & Jackson, I. (2005). The seismological signature of temperature and grain size variations in the upper mantle. *Earth and Planetary Science Letters*, *234*(1-2), 119–134.

Faul, U. H., Toomey, D. R., & Waff, H. S. (1994). Intergranular basaltic melt is distributed in thin, elongated inclusions. *Geophysical Research Letters*, *21*(1), 29–32.

Ferguson, D. J., Maclennan, J., Bastow, I. D., Pyle, D., Jones, S., Keir, D., ... Yirgu, G. (2013). Melting during late-stage rifting in afar is hot and deep. *Nature*, *499*(7456), 70–73.

Ferrando, S., Frezzotti, M., Neumann, E.-R., De Astis, G., Peccerillo, A., Dereje, A., ... Teklewold, A. (2008). Composition and thermal structure of the lithosphere beneath the ethiopian plateau: evidence from mantle xenoliths in basanites, injibara, lake tana province. *Mineralogy and Petrology*, *93*(1), 47–78.

French, S., Lekic, V., & Romanowicz, B. (2013). Waveform tomography reveals channeled flow at the base of the oceanic asthenosphere. *Science*, *342*(6155), 227–230.

French, S., & Romanowicz, B. (2014). Whole-mantle radially anisotropic shear velocity structure from spectral-element waveform tomography. *Geophysical Journal International*, *199*(3), 1303–1327.

Gallacher, R. J., Keir, D., Harmon, N., Stuart, G., Leroy, S., Hammond, J. O., ... others (2016). The initiation of segmented buoyancy-driven melting during continental breakup. *Nature Communications*, *7*(1), 1–9.

Gani, N. D., Gani, M. R., & Abdel Salam, M. G. (2007). Blue nile incision on the ethiopian plateau: Pulsed plateau growth, pliocene uplift, and hominin evolution.

George, R., & Rogers, N. (2002). Plume dynamics beneath the african plate inferred from the geochemistry of the tertiary basalts of southern ethiopia. *Contributions to Mineralogy and Petrology*, *144*(3), 286–304.

Ghiorso, M. S., Hirschmann, M. M., Reiners, P. W., & Kress, V. C. (2002). The pmelts: A revision of melts for improved calculation of phase relations and major element partitioning related to partial melting of the mantle to 3 gpa. *Geochemistry, Geophysics, Geosystems*, *3*(5), 1–35.

Guidarelli, M., Stuart, G., Hammond, J. O., Kendall, J., Ayele, A., & Belachew, M. (2011). Surface wave tomography across afar, ethiopia: Crustal structure at a rift triple-junction zone. *Geophysical Research Letters*, *38*(24).

Hammond, J. O. (2014). Constraining melt geometries beneath the afar depression, ethiopia from teleseismic receiver functions: The anisotropic h-κ stacking technique. *Geochemistry, Geophysics, Geosystems*, *15*(4), 1316–1332.

Hammond, J. O., Kendall, J.-M., Stuart, G., Keir, D., Ebinger, C., Ayele, A., & Belachew, M. (2011). The nature of the crust beneath the afar triple junction: Evidence from receiver functions. *Geochemistry, Geophysics, Geosystems*, *12*(12).

Hammond, W. C., & Humphreys, E. D. (2000). Upper mantle seismic wave velocity: Effects of realistic partial melt geometries. *Journal of Geophysical Research: Solid Earth*, *105*(B5), 10975–10986.

Hart, S. R., & Zindler, A. (1986). In search of a bulk-earth composition. *Chemical Geology*, *57*(3-4), 247–267.

Hastings, W. K. (1970). Monte carlo sampling methods using markov chains and their applications.

Havlin, C., Parmentier, E., & Hirth, G. (2013). Dike propagation driven by melt accumulation at the lithosphere-asthenosphere boundary. *Earth and Planetary Science Letters*, *376*, 20-28. Retrieved from `https://www.sciencedirect.com/science/article/pii/S0012821X13003269` doi: https://doi.org/10.1016/j.epsl.2013.06.010

Hayward, N., & Ebinger, C. (1996). Variations in the along-axis segmentation of the afar rift system. *Tectonics*, *15*(2), 244–257.

Hirth, G., & Kohlstedf, D. (2003). Rheology of the upper mantle and the mantle wedge: A view from the experimentalists. *Geophysical Monograph-American Geophysical Union*, *138*, 83–106.

Hofmann, C., Courtillot, V., Feraud, G., Rochette, P., Yirgu, G., Ketefo, E., & Pik, R. (1997). Timing of the ethiopian flood basalt event and implications for plume birth and global change. *Nature*, *389*(6653), 838–841.

Holtzman, B. K., & Kendall, J. M. (2010). Organized melt, seismic anisotropy, and plate boundary lubrication. *Geophys. Geochem. Geosyst*, *11*, Q0AB06.

Jackson, I., Fitz Gerald, J. D., Faul, U. H., & Tan, B. H. (2002). Grain-size-sensitive seismic wave attenuation in polycrystalline olivine. *Journal of Geophysical Research: Solid Earth*, *107*(B12), ECV–5.

Jin, G., & Gaherty, J. B. (2015). Surface wave phase-velocity tomography based on multichannel cross-correlation. *Geophysical Journal International*, *201*(3), 1383–1398.

Jin, G., Gaherty, J. B., Abers, G. A., Kim, Y., Eilon, Z., & Buck, W. R. (2015). Crust and upper mantle structure associated with extension in the w oodlark r ift, p apua n ew g uinea from r ayleigh-wave tomography. *Geochemistry, Geophysics, Geosystems*, *16*(11), 3808–3824.

Johnson, T. E., Ayalew, T., Mogessie, A., Kruger, F. J., & Poujol, M. (2004). Constraints on the tectonometamorphic evolution of the western ethiopian shield. *Precambrian Research*, *133*(3-4), 305–327.

Julià, J., Ammon, C. J., & Nyblade, A. A. (2005). Evidence for mafic lower crust in tanzania, east africa, from joint inversion of receiver functions and rayleigh wave dispersion velocities. *Geophysical Journal International*, *162*(2), 555–569.

Keir, D., Bastow, I. D., Whaler, K. A., Daly, E., Cornwell, D. G., & Hautot, S. (2009). Lower crustal earthquakes near the ethiopian rift induced by magmatic processes. *Geochemistry, Geophysics, Geosystems*, *10*(6).

Keith, C. M., & Crampin, S. (1977a). Seismic body waves in anisotropic media: propagation through a layer. *Geophysical Journal International*, *49*(1), 209–223.

Keith, C. M., & Crampin, S. (1977b). Seismic body waves in anisotropic media: reflection and refraction at a plane interface. *Geophysical Journal International*, *49*(1), 225–243.

Keith, C. M., & Crampin, S. (1977c). Seismic body waves in anisotropic media: synthetic seismograms. *Geophysical Journal International*, *49*(1), 181–208.

Keranen, K. M., & Klemperer, S. L. (2008). Discontinuous and diachronous evolution of the main ethiopian rift: Implications for development of continental rifts. *Earth and Planetary Science Letters*, *265*(1-2), 96–111.

Keranen, K. M., Klemperer, S. L., Julia, J., Lawrence, J. F., & Nyblade, A. A. (2009). Low lower crustal velocity across ethiopia: Is the main ethiopian rift a narrow rift in a hot craton? *Geochemistry, Geophysics, Geosystems*, *10*(5).

Khan, A., Zunino, A., & Deschamps, F. (2011). The thermo-chemical and physical structure beneath the north american continent from bayesian inversion of surface-wave phase velocities. *Journal of Geophysical Research: Solid Earth*, *116*(B9).

Kieffer, B., Arndt, N., Lapierre, H., Bastien, F., Bosch, D., Pecher, A., ... others (2004). Flood and shield basalts from ethiopia: magmas from the african superswell. *Journal of Petrology*, *45*(4), 793–834.

Korme, T., Acocella, V., & Abebe, B. (2004). The role of pre-existing structures in the origin, propagation and architecture of faults in the main ethiopian rift. *Gondwana Research*, *7*(2), 467–479.

Korme, T., Chorowicz, J., Collet, B., & Bonavia, F. F. (1997). Volcanic vents rooted on extension fractures and their geodynamic implications in the ethiopian rift. *Journal of Volcanology and Geothermal Research*, *79*(3-4), 205–222.

Korostelev, F., Weemstra, C., Leroy, S., Boschi, L., Keir, D., Ren, Y., ... others (2015). Magmatism on rift flanks: Insights from ambient noise phase velocity in afar region. *Geophysical Research Letters*, *42*(7), 2179–2188.

Lavayssière, A., Rychert, C., Harmon, N., Keir, D., Hammond, J. O., Kendall, J.-M., ... Leroy, S. (2018). Imaging lithospheric discontinuities beneath the northern east african rift using s-to-p receiver functions. *Geochemistry, Geophysics, Geosystems*, *19*(10), 4048–4062.

Ligorría, J. P., & Ammon, C. J. (1999). Iterative deconvolution and receiver-function estimation. *Bulletin of the seismological Society of America*, *89*(5), 1395–1400.

Lin, F.-C., & Ritzwoller, M. H. (2011). Helmholtz surface wave tomography for isotropic and azimuthally anisotropic structure. *Geophysical Journal International*, *186*(3), 1104–1120.

Lin, F.-C., Ritzwoller, M. H., & Snieder, R. (2009). Eikonal tomography: surface wave tomography by phase front tracking across a regional broad-band seismic array. *Geophysical Journal International*, *177*(3), 1091–1110.

Mackenzie, G., Thybo, H., & Maguire, P. (2005). Crustal velocity structure across the main ethiopian rift: results from two-dimensional wide-angle seismic modelling. *Geophysical Journal International*, *162*(3), 994–1006.

Maguire, P., Keller, G., Klemperer, S., Mackenzie, G., Keranen, K., Harder, S., ... Khan,

M. (2006). Crustal structure of the northern main ethiopian rift from the eagle controlled-source survey; a snapshot of incipient lithospheric break-up. *Geological Society, London, Special Publications*, *259*(1), 269–292.

Masters, G., Barmine, M., & Kientz, S. (2007). Mineos user's manual in computational infrastructure for geodynamics. *Calif. Inst. of Technol., Pasadena*.

Meert, J. G., & Lieberman, B. S. (2008). The neoproterozoic assembly of gondwana and its relationship to the ediacaran–cambrian radiation. *Gondwana research*, *14*(1-2), 5–21.

Mège, D., & Korme, T. (2004). Dyke swarm emplacement in the ethiopian large igneous province: not only a matter of stress. *Journal of Volcanology and Geothermal Research*, *132*(4), 283–310.

MELT Seismic Team, T. (1998). Imaging the deep seismic structure beneath a mid-ocean ridge: The melt experiment. *Science*, *280*(5367), 1215–1218.

Menke, W., & Levin, V. (2003). The cross-convolution method for interpreting sks splitting observations, with application to one and two-layer anisotropic earth models. *Geophysical Journal International*, *154*(2), 379–392.

Metropolis, N., Rosenbluth, A. W., Rosenbluth, M. N., Teller, A. H., & Teller, E. (1953). Equation of state calculations by fast computing machines. *The journal of chemical physics*, *21*(6), 1087–1092.

Mohamed, A. Y., Ashcroft, W., & Whiteman, A. (2001). Structural development and crustal stretching in the muglad basin, southern sudan. *Journal of African Earth Sciences*, *32*(2), 179–191.

Ogden, C., Bastow, I. D., Gilligan, A., & Rondenay, S. (2019). A reappraisal of the h–κ stacking technique: implications for global crustal structure. *Geophysical Journal International*, *219*(3), 1491–1513.

Oliver, J. (1962). A summary of observed seismic surface wave dispersion. *Bulletin of the Seismological Society of America*, *52*(1), 81–86.

Orfanos, C., Leontarakis, K., Lois, A., Polychronopoulou, K., & Martakis, N. (2016). Automatic passive seismic data processing with no prior information: the contribution of surface wave tomography. *first break*, *34*(7).

Pik, R., Marty, B., Carignan, J., Yirgu, G., & Ayalew, T. (2008). Timing of east african rift development in southern ethiopia: Implication for mantle plume activity and evolution of topography. *Geology*, *36*(2), 167–170.

Pratt, M. J., Wysession, M. E., Aleqabi, G., Wiens, D. A., Nyblade, A. A., Shore, P., ... others (2017). Shear velocity structure of the crust and upper mantle of madagascar derived from surface wave tomography. *Earth and Planetary Science Letters*, *458*, 405–417.

Rooney, T. O., Bastow, I. D., Keir, D., Mazzarini, F., Movsesian, E., Grosfils, E. B., ... Yirgu, G. (2014). The protracted development of focused magmatic intrusion during continental rifting. *Tectonics*, *33*(6), 875–897.

Rooney, T. O., Herzberg, C., & Bastow, I. D. (2012). Elevated mantle temperature beneath east africa. *Geology*, *40*(1), 27–30.

Rooney, T. O., Lavigne, A., Svoboda, C., Girard, G., Yirgu, G., Ayalew, D., & Kappelman, J. (2017). The making of an underplate: Pyroxenites from the ethiopian lithosphere. *Chemical Geology*, *455*, 264–281.

Roy, C., & Romanowicz, B. (2017). On the implications of a priori constraints in transdimensional bayesian inversion for continental lithospheric layering. *Journal of Geophysical Research: Solid Earth*, *122*(12), 10–118.

Rychert, C. A., Hammond, J. O., Harmon, N., Kendall, J. M., Keir, D., Ebinger, C., ... Stuart, G. (2012). Volcanism in the afar rift sustained by decompression melting with minimal plume influence. *Nature Geoscience*, *5*(6), 406–409.

Shackleton, R. (1986). Precambrian collision tectonics in africa. *Geological Society, London, Special Publications*, *19*(1), 329–349.

Shen, W., Ritzwoller, M. H., Schulte-Pelkum, V., & Lin, F.-C. (2013). Joint inversion of surface wave dispersion and receiver functions: a bayesian monte-carlo approach. *Geophysical Journal International*, *192*(2), 807–836.

Stern, R. J., Nielsen, K. C., Best, E., Sultan, M., Arvidson, R. E., & KrÃ¶ner, A. (1990). Orientation of late precambrian sutures in the arabian-nubian shield. *Geology*, *18*(11), 1103–1106.

Stuart, G., Bastow, I. D., & Ebinger, C. (2006). Crustal structure of the northern main ethiopian rift from receiver function studies. *Geological Society, London, Special Publications*, *259*(1), 253–267.

Takei, Y. (2017). Effects of partial melting on seismic velocity and attenuation: A new insight from experiments. *Annual Review of Earth and Planetary Sciences*, *45*, 447–470.

Ukstins, I. A., Renne, P. R., Wolfenden, E., Baker, J., Ayalew, D., & Menzies, M. (2002). Matching conjugate volcanic rifted margins: 40ar/39ar chrono-stratigraphy of pre-and syn-rift bimodal flood volcanism in ethiopia and yemen. *Earth and Planetary Science Letters*, *198*(3-4), 289–306.

Vail, J. R. (1985). Pan-african (late precambrian) tectonic terrains and the reconstruction of the arabian-nubian shield. *Geology*, *13*(12), 839–842.

Weeraratne, D. S., Forsyth, D. W., Fischer, K. M., & Nyblade, A. A. (2003). Evidence for an upper mantle plume beneath the tanzanian craton from rayleigh wave tomography. *Journal of Geophysical Research: Solid Earth*, *108*(B9).

White, R., & McKenzie, D. (1995). Mantle plumes and flood basalts. *Journal of Geophysical Research: Solid Earth*, *100*(B9), 17543–17585.

Woldegabriel, G., Aronson, J. L., & Walter, R. C. (1990). Geology, geochronology, and rift basin development in the central sector of the main ethiopia rift. *Geological Society of America Bulletin*, *102*(4), 439–458.

Wolfenden, E., Ebinger, C., Yirgu, G., Deino, A., & Ayalew, D. (2004). Evolution of the northern main ethiopian rift: birth of a triple junction. *Earth and Planetary Science Letters*, *224*(1-2), 213–228.

Zhu, L., & Kanamori, H. (2000). Moho depth variation in southern california from teleseismic receiver functions. *Journal of Geophysical Research: Solid Earth*, *105*(B2), 2969–2980.

EARS_map.


a)
b)
Phv Station
Group 1
Group 2
Group 3
5mm
DAQU
MGNA
SERE
MELA
MUKA
SHAW
BAHI
JAWI
ABMD
GUBL
CHGE
GUBA
DEBR
SHER
HARO
KIRE
MERT
ASOS
MEND
HDBU
NEKE
GIDA
GORE
JIMA
AMME
ARBA
CHEF
DLMN
Blue Nile Rift
Lake Tana
Ogaden Rift
Flood Basalt
Faults
Holocene Volcanoes
Mio-Plio Volcanoes
Quaternary Strombolians
Fumaroles
Thermal Springs
16
14
12
10
8
6
4
34
36
38
40
42
44
3000
2500
2000
1500
1000
500
0

KIRE_DBQC_plot.

a)
b)
c)
d)
Time, s
-5
0
5
10
15
20
25
-0.5
0
0.5
1
Amplitude
Amplitude
Amplitude

GUBA_allHK.


a)
True Daughter RF
Predicted Daughter RF
Amplitude
Time, s
b)
True Phase Velocity
Predicted Phase Velocity
Phase Velocity, km/s
Period, s
c)
Mean Best Predicted H-κ
Best fit per model
Moho depth
Vp/Vs ratio
Normalized Stack Amplitude

Phase_vel_all_periods.


a) 25 s
b) 32 s
c) 40 s
d) 50 s
e) 60 s
f) 80 s
34
36
38
40
42
44
16
14
12
10
8
6
4
3.5
3.6
3.7
3.8
3.9
4

F67_Moho_Vs_scatter.


0.8 km
2 km
3.6 km
Moho Depth, km
a)
b) 30 km
δ Vs (%)
Vs (km/s)
c) 50 km
d) 70 km
e) 110 km
δ Vs (%)
Vs (km/s)

F9_regionalized_VS.


Group 1
Group 2
Group 3
Comparison
Depth (km)
Vs (km/s)
a)
b)
c)
d)
20
40
60
80
100
120
140
3.6
3.8
4
4.2
4.4
3.5
4.5
Group 1
Group 2
Group 3
PREM
MOR
L Proter
E Proter
Moz. Belt

Melt_temp_geotherm.

Melt (%)
0
1
2
3
a)
Dry Perid.
Group 1
Group 2
Group 3
Dry Per.
Depth (km)
Temperature (°C)
b)
pMELTS
P = 3 GPa (~90 km)
-10% δVs
-8% δVs
-6% δVs
-4% δVs
-2% δVs
Melt (%)
Temperature (°C)

Distributed Extension across the Ethiopian Rift and Plateau Illuminated by Joint Inversion of Surface Waves and Scattered Body Waves

J. Petruska[1], Z. Eilon [1]

[1]University of California, Santa Barbara

Contents of this file

1. Table T1
2. Text S1 to S5
3. Figures S1 to S12

Additional Supporting Information (Files uploaded separately)

1. Data fit images S12 to S92
2. RF quality control images S93 - S120

Introduction Below we present several figures to support observations and conclusions we develop in the main document. All data are developed from the same two data sets presented in the main document, and figures presented show interim steps that may clarify decisions made during interpretation. Figure S1 shows the raw H-κ derived Moho and Vp/Vs results. Figures S2 - S7 seek to show inherent difficulty and error in forward

---

Corresponding author: J. Petruska, , Department of Earth Science, University of California, Santa Barbara, 1006 Webb Hall, Santa Barbara, CA, 93106, USA. (jonpetruska@ucsb.edu)

modelling geotherms into shear velocities. S8 - S10 display results used for interpretation, that were not included in the main document due to size constraints. Figure S11 displays a test modified from the methodology of Ogden, Bastow, Gilligan, and Rondenay (2019), comparing the results of H-κ stacking before and after quality controls. Zipped files contain results seen in S8 - S10, and S11 for each station inverted for shear velocity.

Receiver Function Derived Crustal Thickness and Vp/Vs Ratios S1. Crustal thickness and Vp/Vs ratios are taken as the maximum of the normalized H-κ surface at each station. A Vp of 6.3 is used, and phase weights of 0.7, 0.2, 0.1 are used in the H-κ stacking process. Crustal thickness results are similar to those of the inverted results, and trends discussed in the inverted crustal thickness section are relevant here as well. Our Vp/Vs ratios are similar to those of (Hammond et al., 2011) in the western Ethiopian Plateau (1.7 - 1.9). There is broader uncertainty with the Vp/Vs ratio than the crustal thickness, even for well constrained H-κ stack surfaces, as can be seen below in the inversion data fit subsection.

Geotherm Gridsearch Considerations S2.

It is difficult to forward model shear velocities from a continental geotherm that can closely predict shear velocities using existing scaling relationships (Dalton & Faul, 2010). Cammarano, Goes, Deuss, and Giardini (2005); Cammarano and Romanowicz (2007) discuss the difficulties in matching velocity models from geophysical observations and compositional, thermal, and anisotropic effects in the Earth. Calculating a shear velocity profile from geotherms cannot, as far as we currently understand it, perfectly predict shear velocity structures. Using different forward modeling methods, with the same input geotherm, can produce shear velocities at the same depth as different as $\sim$0.4 km/s. To calculate shear velocities, we use calculations from (Takei, 2017; Jackson & Faul, 2010; Faul & Jackson, 2005; Priestley & McKenzie, 2013) and an anharmonic calculation to show variance between these methods.

Deviation between observed and modeled Vs are most apparent between 30 and 60 km, where the geotherms change slope to an adiabatic gradient. Determining how to better forward model shear velocities from a geotherm is beyond the scope of this research, so we instead use a geotherm gridsearch, minimizing misfit between predicted and observed Vs between 60 and 120 km, the depths our phase velocity data are most sensitive.

Geotherm Parameter Gridsearch S3. Because of the inherent difficulty in perfectly matching shear velocity observations forward modeled from a geotherm, we gridsearch crustal thickness, mantle potential temperature (T_m), surface heat flow (Q_0), and radiogenic heat production (A_0). This determines a range of parameters that produce well-fit shear velocity models by minimizing the misfit between the forward modeled geotherm and the observed shear velocity of each group. Because of the notable spread in shear velocity estimates seen above, we chose to use a single method during gridsearching, Takei (2017), as this method generally provided better fits to the observed shear velocities. Note that we do not show the results of crustal thickness, as we found our geotherms insensitive to it.

Inversion Data Fit and H-κ stacks S4. For each station we jointly inverted, we have included three images similar to figure 4 in the manuscript. The naming scheme is as follows, where STATION NAME refers to the inverted station. STATION NAME_data_pred.jpg : The fit of the mean surface wave, receiver function, and H-κ model. STATION NAME_HK_fit.jpg : The same as the previous image, but with every H-κ solution from shear velocity models plotted in the gridsearch area. STATION NAME_vs_prof.jpg : The inverted shear velocity profile. The red line indicates the mean model, the grey patch is the 1σ, and white patch bounded in light grey is the 2σ. The posterior distribution of Moho solutions is plotted as a red histogram, and the best fit Moho depth and standard deviation are denoted by the horizontal dashed black line. An example of the three images is shown below for clarification.

H-κ Reliability Test S5. Ogden et al. (2019) found that many H-κ derived estimates were unreliable within the EPL. Using an automatic method to perturb input parameters for H-κ stacking, they found that stations within flood basalts produced unreliable H-κ stacks with high standard deviation, low SNR, and broad low amplitude arrival phases. Such H-κ stacks failed to resolve a high energy maximum for the Moho and κ due to a gradational Moho, complex crust, or sediments and basalts.

To test the reliability our H-κ stack results, we modified Ogden et al. (2019)'s random input perturbation procedure on several stations in the region using receiver functions from before the DBSCAN process (raw) and those that passed the DBSCA process (cleaned). We randomly perturbed the Vp from [6.2: 0.1: 6.8], the maximum filter frequency from [0.1: 0.1: 2.0] Hz before calculating the receiver function, the weight of the Ps phase from [0.4: 0.05: 0.9], the $PpPs$ phase from [0.1: 0.05: 0.6], and the $PpSs + PsPs$ phase from [0.0: 0.05: 0.5] (with total phase weights required to sum to 1.0). These random perturbations were run 5000 times for the raw and cleaned receiver functions. A robust result was expected to display a distinct high energy maximum in the H-κ surface, closely clustered mean model solutions between different input parameters, a similar mean and mode H-κ for all 5000 models, and an H and κ that were not capped at the edges of the grid search surface. An example of this process is shown in fig. S11. Raw H-κ stack surfaces (fig. S11a) generally fail to find a high energy maximum - the summation of all H-κ surfaces finds five high energy maxima in which input parameter variability solved to different maxima despite using the same data. The mean H-κ value of the 5000 iterations (40.81, 1.81) is dissimilar to the absolute maximum of the surface (39.9, 1.6). The surface maximum is also capped by the bounds of the κ values. Contrarily, the cleaned H-κ stack surface (fig. S11b) finds a well defined maximum in the H-κ stack surface (37.4, 1.68), which is similar to the mean (37.52, 1.67) of the 5000 best fit H-κ iterations. We note that the difference between raw and cleaned H-κ stack surfaces are not consistently different across all stations, but quality controls still improved the H-κ energy surface. **T1. Moho Depth Table**

Station	Moho (km)	Std (km)	Lat	Lon
ABMD	29.25	1.52	11.832	35.583
AMME	37.80	1.41	8.303	39.093
ARBA	28.06	1.76	6.067	37.556
ASOS	33.06	2.10	10.091	34.564
BAHI	35.30	1.70	11.574	37.393
CHEF	31.29	1.44	6.161	38.210
CHGE	34.04	2.86	10.961	36.518
DAQU	32.79	1.24	13.145	37.898
DEBR	27.98	1.52	10.635	35.662
DLMN	36.86	3.22	6.424	39.856
GIDA	34.02	2.42	8.980	34.610
GORE	34.34	1.87	8.150	35.533
GUBA	28.52	1.32	11.271	35.289
GUBL	32.58	1.20	11.179	36.005
HARO	32.00	1.28	9.847	36.310
HDBU	34.55	0.84	9.376	35.651
JAWI	31.48	1.28	11.571	36.491
JIMA	30.88	3.65	7.684	36.831
KIRE	37.23	1.63	9.957	36.869
MELA	28.37	1.44	12.396	35.960

continued on next page

MEND	31.81	0.96	9.787	35.111
MERT	36.59	1.71	10.876	38.266
MGNA	28.80	1.77	12.786	36.404
MUKA	31.89	1.02	12.064	36.374
NEKE	31.22	1.03	9.089	36.523
SERE	38.96	1.89	12.513	37.028
SHAW	33.99	2.13	11.930	36.870
SHER	31.28	1.01	10.594	34.786

Table S1: ds12. A list of Moho thicknesses and standard deviation, in km, from post-inversion shear velocity models.

S1. Moho and Vp/Vs ratio

S2. - S4. Forward modeled Vs from Geotherms

S5. Geotherm Gridsearch Misfits for Group 1

S6. Geotherm Gridsearch Misfits for Group 2

S7. Geotherm Gridsearch Misfits for Group 3

S8. Predicted and Observed Data fit

S9. Predicted and Observed Data fit, H-κ Models

S10. Shear Velocity Model and Moho Distribution

S11. H-κ Stack Testing

References

Cammarano, F., Goes, S., Deuss, A., & Giardini, D. (2005). Is a pyrolitic adiabatic mantle compatible with seismic data? *Earth and Planetary Science Letters*, *232*(3-4), 227–243.

Cammarano, F., & Romanowicz, B. (2007). Insights into the nature of the transition zone from physically constrained inversion of long-period seismic data. *Proceedings of the National Academy of Sciences*, *104*(22), 9139–9144.

Dalton, C. A., & Faul, U. H. (2010). The oceanic and cratonic upper mantle: Clues from joint interpretation of global velocity and attenuation models. *Lithos*, *120*(1-2), 160–172.

Faul, U. H., & Jackson, I. (2005). The seismological signature of temperature and grain size variations in the upper mantle. *Earth and Planetary Science Letters*, *234*(1-2), 119–134.

Hammond, J. O., Kendall, J.-M., Stuart, G., Keir, D., Ebinger, C., Ayele, A., & Belachew, M. (2011). The nature of the crust beneath the afar triple junction: Evidence from receiver functions. *Geochemistry, Geophysics, Geosystems*, *12*(12).

Jackson, I., & Faul, U. H. (2010). Grainsize-sensitive viscoelastic relaxation in olivine: Towards a robust laboratory-based model for seismological application. *Physics of the Earth and Planetary Interiors*, *183*(1-2), 151–163.

Ogden, C., Bastow, I. D., Gilligan, A., & Rondenay, S. (2019). A reappraisal of the h–κ stacking technique: implications for global crustal structure. *Geophysical Journal International*, *219*(3), 1491–1513.

Priestley, K., & McKenzie, D. (2013). The relationship between shear wave velocity, temperature, attenuation and viscosity in the shallow part of the mantle. *Earth and Planetary Science Letters*, *381*, 78–91.

Takei, Y. (2017). Effects of partial melting on seismic velocity and attenuation: A new insight from experiments. *Annual Review of Earth and Planetary Sciences*, *45*, 447–470.

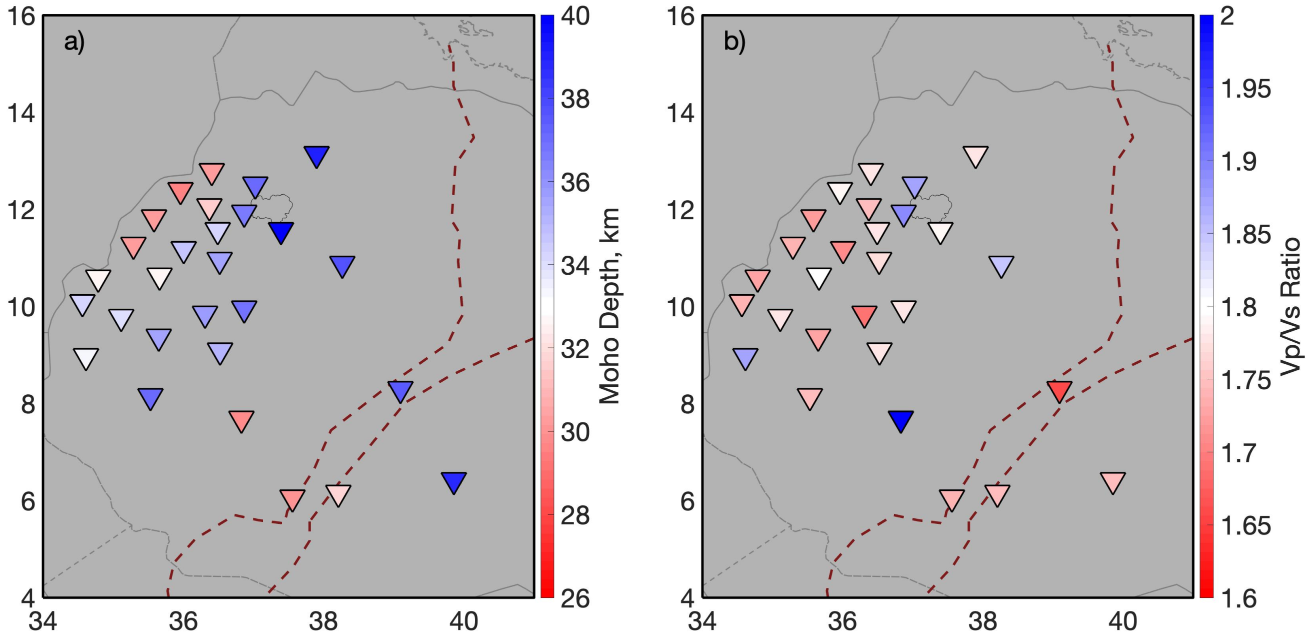

Figure S1. ds01.a) The crustal thicknesses for each station taken as the maximum energy region in the H-κ surface. Warmer colors indicate shallower crust. ds01.b) The Vp/Vs ratio from the same H-κ surface, at each station. Warmer colors indicate a lower Vp/Vs ratio.

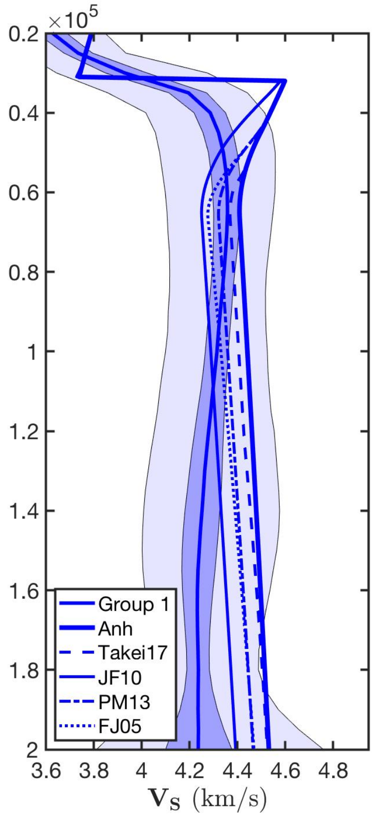

Figure S2. ds02.) The range of modeled Vs by varied methods, of the geotherm best fit to group 1. The group 1 velocity aggregate is plotted in solid dark blue, surrounded by its 1σ (dark blue patch) and 2σ (light blue patch). The anharmonic calculation is also plotted in solid dark blue, but is always faster than the velocity profile. Calculated Vs from (?, ?) are in dashed blue, (Jackson & Faul, 2010) in thin solid blue, (Priestley & McKenzie, 2013) in blue dash-hatches, and (Faul & Jackson, 2005) in blue dots.

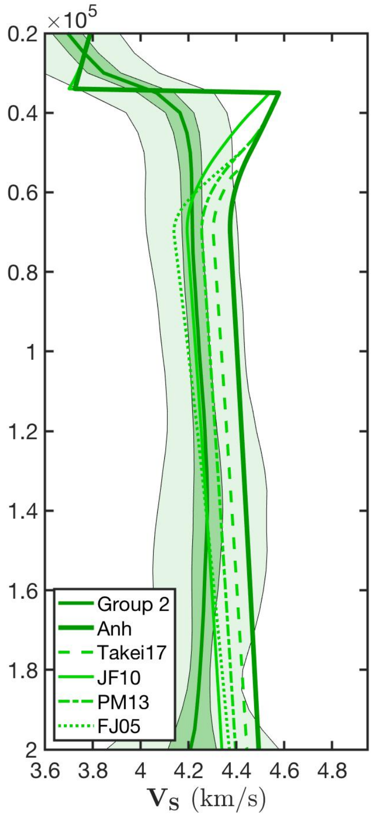

Figure S3. ds03.) The range of modeled Vs by varied methods, of the geotherm best fit to group 2. The group 2 velocity aggregate is plotted in solid dark green, surrounded by its 1σ (dark green patch) and 2σ (light green patch). The anharmonic calculation is also plotted in solid dark green, but is always faster than the velocity profile. Calculated Vs from (?, ?) are in dashed green, (Jackson & Faul, 2010) in thin solid green, (Priestley & McKenzie, 2013) in green dash-hatches, and (Faul & Jackson, 2005) in green dots.

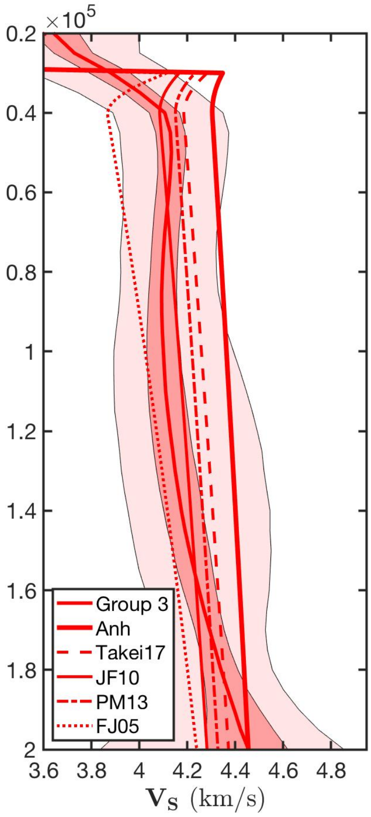

Figure S4. ds04.) The range of modeled Vs by varied methods, of the geotherm best fit to group 3. The group 3 velocity aggregate is plotted in solid dark red, surrounded by its 1σ (dark red patch) and 2σ (light red patch). The anharmonic calculation is also plotted in solid dark red, but is always faster than the velocity profile. Calculated Vs from (?, ?) are in dashed red, (Jackson & Faul, 2010) in thin solid red, (Priestley & McKenzie, 2013) in red dash-hatches, and (Faul & Jackson, 2005) in red dots.

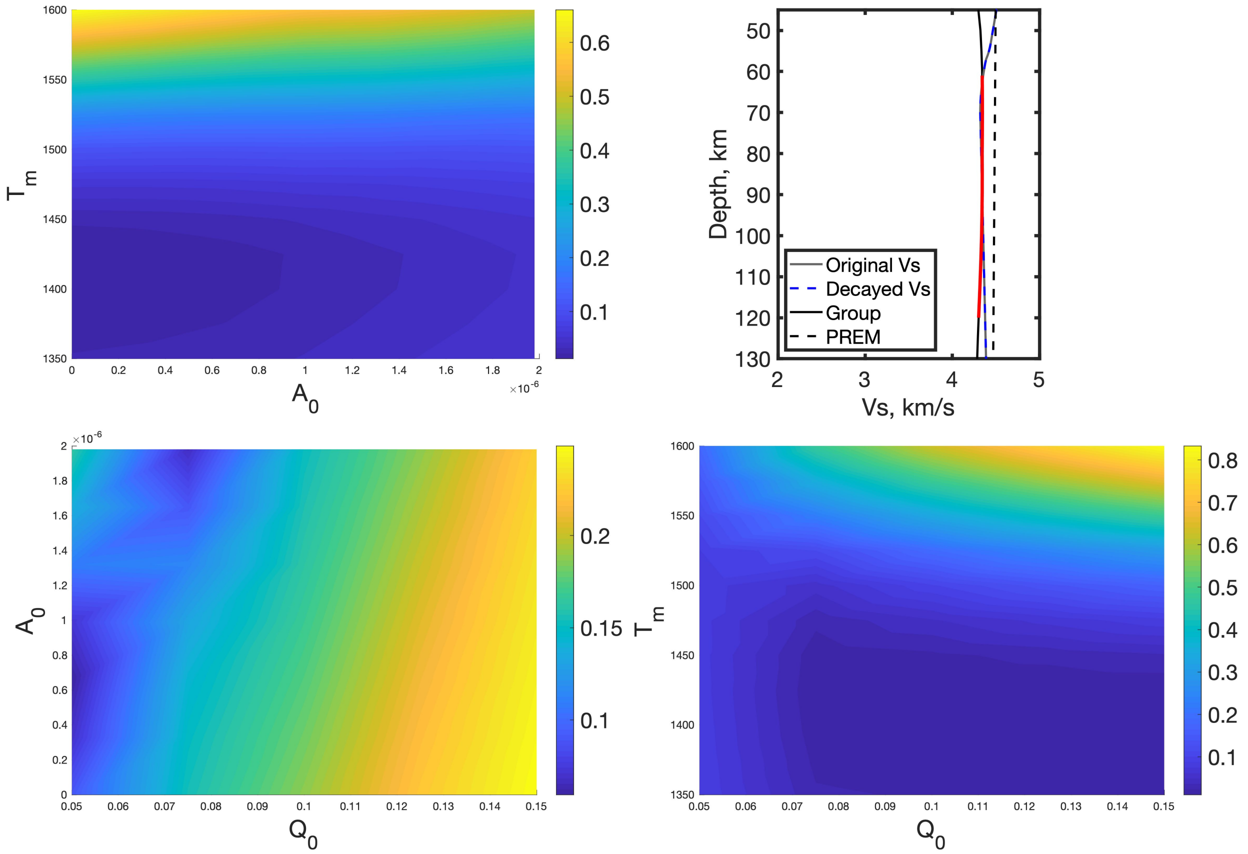

Figure S5. ds05. Misfit surface for Group 1, comparing mantle potential temperatures (T_m), surface heat flow (Q_0) and crustal radiogenic heat production (A_0). Cooler colors indicate lower misfit, warmer colors indicate higher misfit. The shear velocity profile of group 1 (black) is shown in the upper right corner, with the best fit velocity profile before percolation and compaction (grey), and after (dashed blue). PREM is dashed in black, and the depth range used to minimize misfit is highlighted in red on the grou Vs profile.

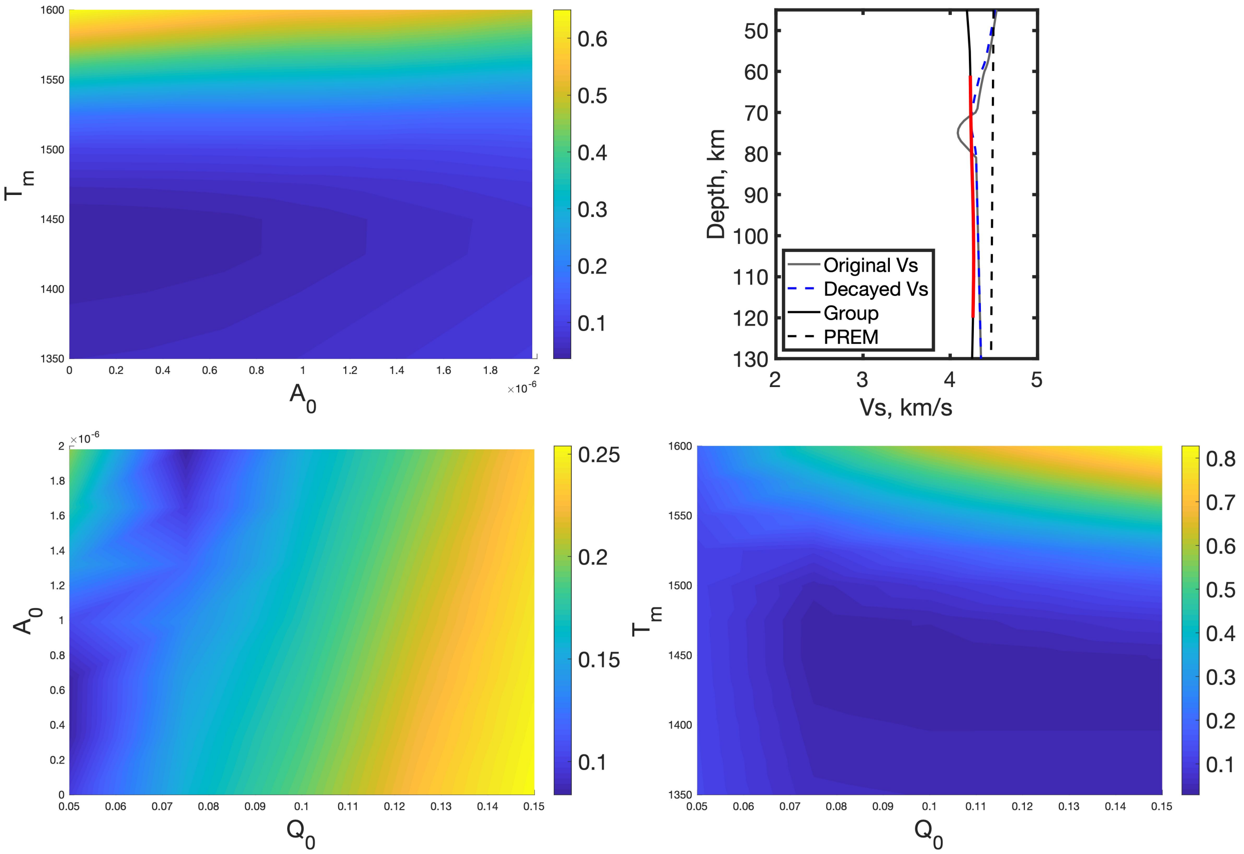

Figure S6. ds06. Misfit surface for Group 2 comparing mantle potential temperatures (T_m), surface heat flow (Q_0) and crustal radiogenic heat production (A_0). Cooler colors indicate lower misfit, warmer colors indicate higher misfit. The shear velocity profile of group 2 (black) is shown in the upper right corner, with the best fit velocity profile before percolation and compaction (grey), and after (dashed blue). PREM is dashed in black, and the depth range used to minimize misfit is highlighted in red on the grou Vs profile.

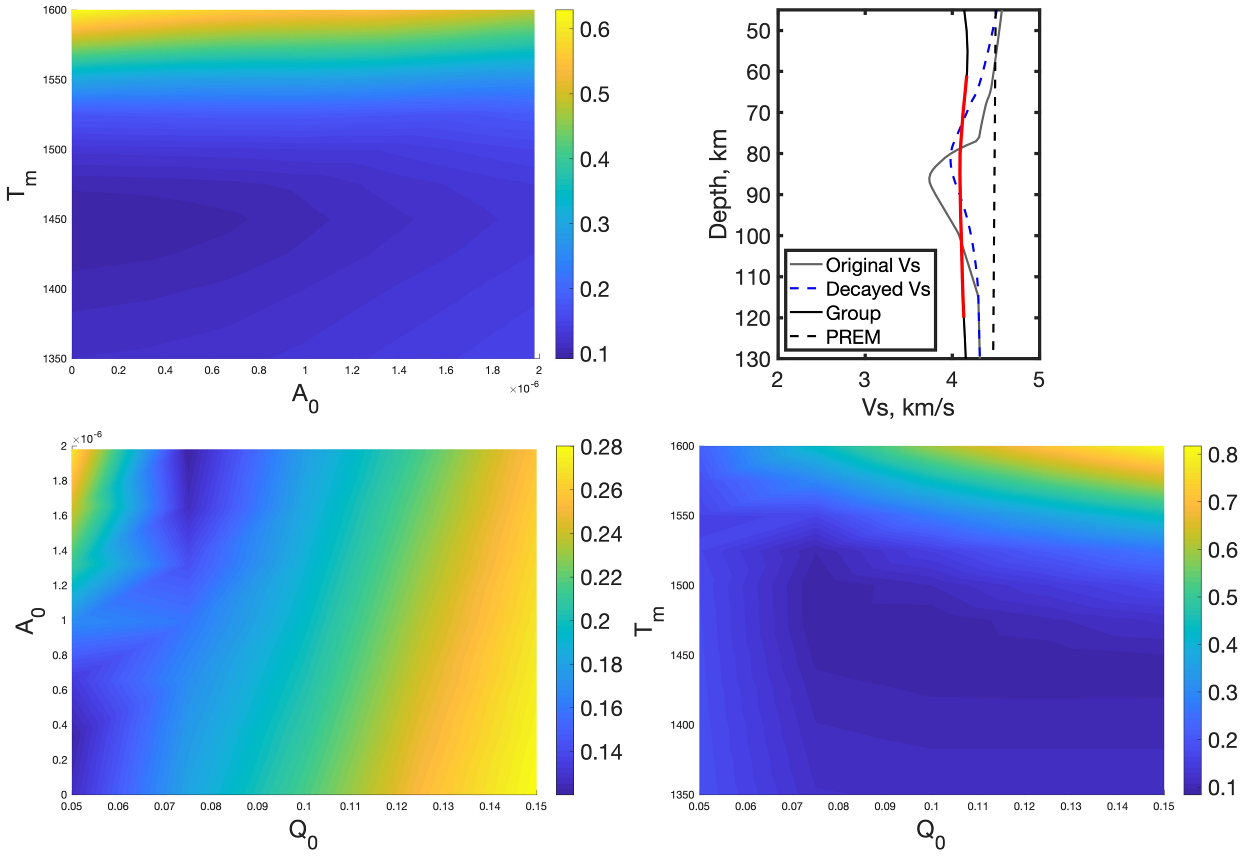

Figure S7. ds07. Misfit surface for Group 3 comparing mantle potential temperatures (T_m), surface heat flow (Q_0) and crustal radiogenic heat production (A_0). Cooler colors indicate lower misfit, warmer colors indicate higher misfit. The shear velocity profile of group 3 (black) is shown in the upper right corner, with the best fit velocity profile before percolation and compaction (grey), and after (dashed blue). PREM is dashed in black, and the depth range used to minimize misfit is highlighted in red on the grou Vs profile.

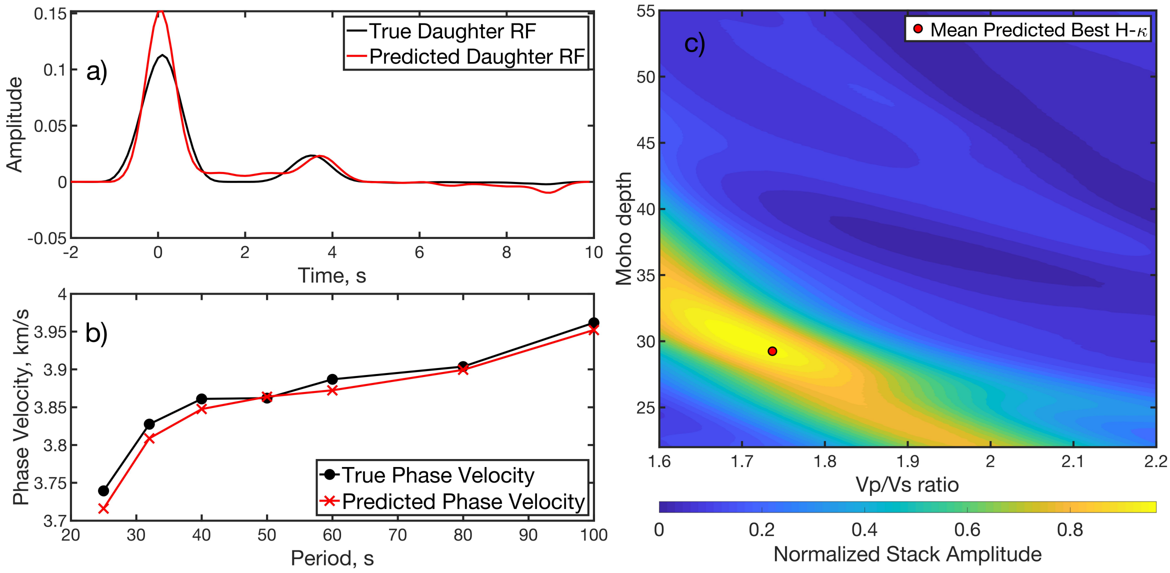

Figure S8. ds08. a) The predicted and observed receiver function data for station ABMD. The observed receiver function is shown in black, the mean of the ensemble of well-fit models is shown in red. b) The observed surface waves (black) and predicted (red) surface waves. c) The H-κ surface after normalization. Warmer colors indicate higher amplitudes. The H-κ result of the mean model is plotted in red.

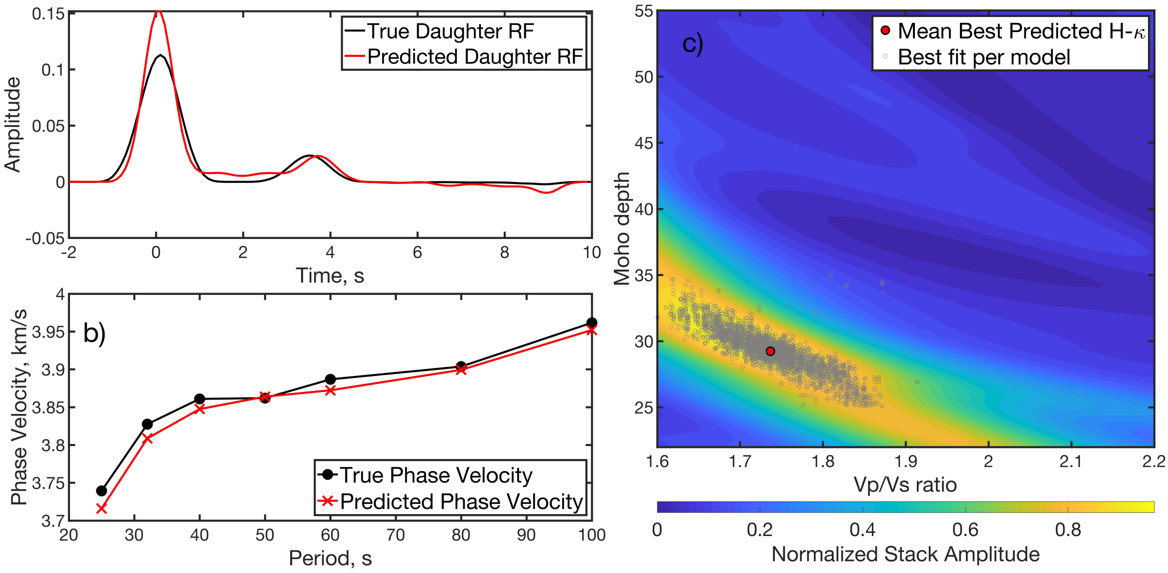

Figure S9. ds09. The same figure as above, but c) now contains the H-κ of all fit models developed during inversion. Light grey circles denote a single model.

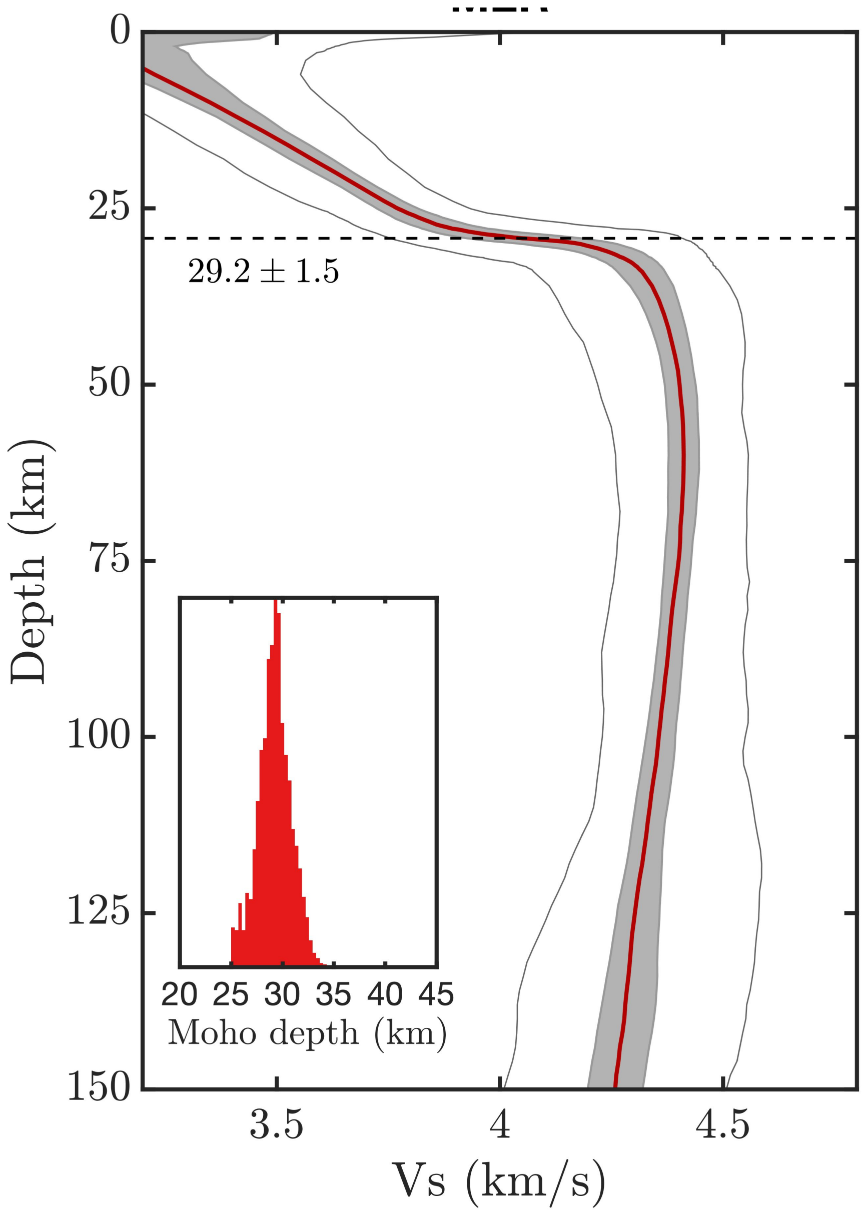

Figure S10. ds10. The shear velocity model of station ABMD. The mean velocity model is plotted in red, the 1σ patched in grey, and the 2σ patched in white bounded by light grey. The histogram of Moho depths is shown in the bottom left. The maximum of the Moho distribution and distribution standard deviation are labelled and displayed as a dashed horizontal black line.

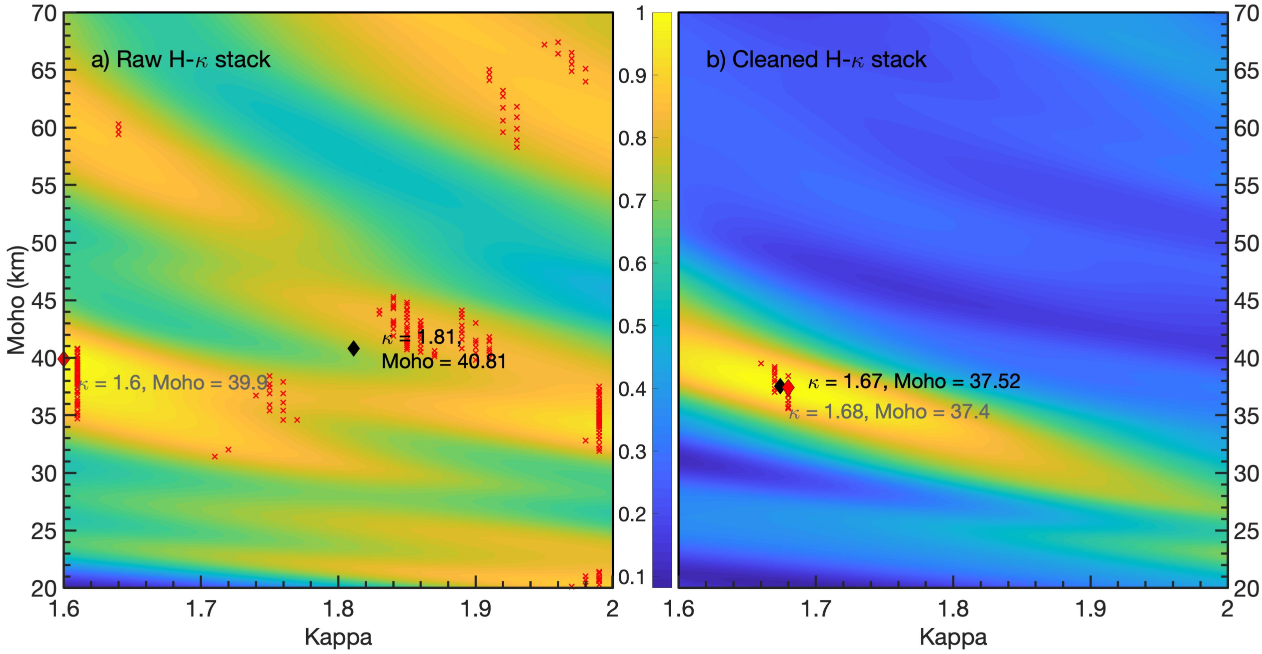

Figure S11. ds11. The results of the cleaned vs raw H-κ stacking procedure. a) shows the results of 5000 H-κ model iterations with randomly perturbed parameters. The red crosses are the best fit H-κ value for a single model iteration. The black diamond is the mean of those models, with corresponding κ and Moho values labelled in black. The red diamond (at the left edge of the surface) is the maximum of the error surface, with the corresponding κ and Moho values labelled in grey. b) shows the results of 5000 H-κ model iterations with randomly perturbed parameters after the DBSCAN process. The black diamond is the mean of those models, with the corresponding κ and Moho values labelled in black. The red diamond is the maximum of the error surface, with the corresponding κ and Moho values labelled in grey. The summed H-κ surfaces are shown in the background for both the raw and cleaned stacks, color coded by the same normalized amplitude scale.